Key Points:
1. Peak delay times of *S* waves are calculated to study the scattering strength in southern Aegean
2. Spectral density of inhomogeneous medium is modeled as von Kármán type and its parameters are evaluated by inverting peak delay times
3. High inhomogeneity zones are observed in Cyclades, Crete, and upper crust of Peloponnese

Correspondence to:
P. Ranjan,
pratulranjan@g.ncu.edu.tw

Spatial Distribution of Random Velocity Inhomogeneities in the Southern Aegean From Inversion of *S* Wave Peak Delay Times

P. Ranjan[1,2] (iD), **K.I. Konstantinou**[2] (iD), **and R. Andinisari**[2] (iD)

[1]Taiwan International Graduate Program- Earth System Science (TIGP-ESS), Taipei, Taiwan, [2]Department of Earth Sciences, National Central University, Chungli, Taoyuan, Taiwan

Abstract The southern Aegean is characterized by an ongoing process of oceanic subduction. In this study, 1,718 intermediate depth (>35 km) events recorded in the southern Aegean are used to calculate the peak delay times (t_p). The t_p are measured as the time difference between *S* wave onset and the peak of the *S* wave envelope in 2-to 4-, 4- to 8-, 8- to 16-, and 16- to 32-Hz bands. The t_p are also inverted to estimate the scattering parameters (κ and $\varepsilon_{\text{param}}$) and power spectral density function (P (m)) at large wave numbers ($m = 15$ km^{-1} or m_l) of the medium modeled as von Kármán type. κ controls frequency dependence of scattering while $P(m_l)$ represents the scattering strength in high frequencies for $am_l >> 1$ (a = correlation length of inhomogeneities). High $P(m_l)$ with low κ across Peloponnese in 0- to 20-km depth may result from intermixing of oceanic material with continental rocks at different levels with a possibility of fluid activity and salt diapirism in northwest Peloponnese. Moderate $P(m_l)$ in 0- to 60-km depth across Crete is likely due to a combination of factors including past megathrust earthquakes, sediment underplating, and flow of metamorphosed material in a subduction channel. Cyclades shows low κ in 0- to 40-km depth, indicative of inhomogeneities produced by metamorphic core complexes. Very low κ in 60- to 80-km depth is consistent with the location of mantle magma reservoir in the back-arc region. Our results suggest that a significant portion of total *S* wave attenuation (Q_s^{-1}) in eastern Cyclades for 20- to 80-km depth may be due to scattering losses.

1. Introduction

The Hellenic Subduction Zone (HSZ) is formed as a result of the northward movement of the Nubian (African) oceanic slab with respect to the Aegean continental microplate followed by subduction in an arc-shaped pattern along Peloponnese in the west, Crete in the south, and Rhodes in the east (Figure 1). The southwestward (SW) movement of the overriding Aegean lithosphere relative to Nubia (35 mm/year) is much faster than 10 mm/year convergence rate between Nubia and Eurasia (Doglioni et al., 2002; McClusky et al., 2000; Reilinger et al., 2006), and this SW movement is largely attributed to the rollback of the Nubian slab. The slab rollback is also believed to be the mechanism behind the extension in the Aegean crust resulting in crustal thinning and formation of the Aegean Sea (Konstantinou et al., 2017; Reilinger et al., 2010) and generation of shallow normal faults throughout the region (Armijo et al., 1992; Stewart & Hancock, 1991). Some of these faults in the Cyclades crust are also linked to the deeper ductile shear zones that formed at the onset of extension in the Aegean crust during late Oligocene-Miocene. These ductile shear zones allowed the exhumation of high-pressure low-temperature metamorphosed middle and lower crustal layers as metamorphic core complexes (MCC; Brun & Faccenna, 2008; Huet et al., 2011; Keay et al., 2001; Lister et al., 1984). The slab rollback has also caused the southward shift of the volcanic front to its current position at the southern boundary of the Cyclades. Some of its volcanoes have active magma chambers and show strong fluid-induced seismic activity episodically (Feuillet, 2013; Foutrakis & Anastasakis, 2018; Konstantinou et al., 2013; Marini et al., 1993). Seismicity studies along the HSZ also reveal a broad pattern. Shallow earthquakes (<20 km) in the overriding Aegean plate are mainly due to extension. Maximum depth of low-angle thrust earthquakes on the subduction interface changes from 15 km in Peloponnese to 45 km in the central HSZ near Crete. Shallow steeply dipping splay faulting above the interface has also produced large earthquakes that may have generated part of the uplift observed in Crete. Wadati-Benioff zone studies reveal a change in the dip of the slab from 30° in the 20- to 100-km depth beneath the forearc to 45° in the 100- to 180-km depth beneath the backarc (Hatzfeld et al., 1993;
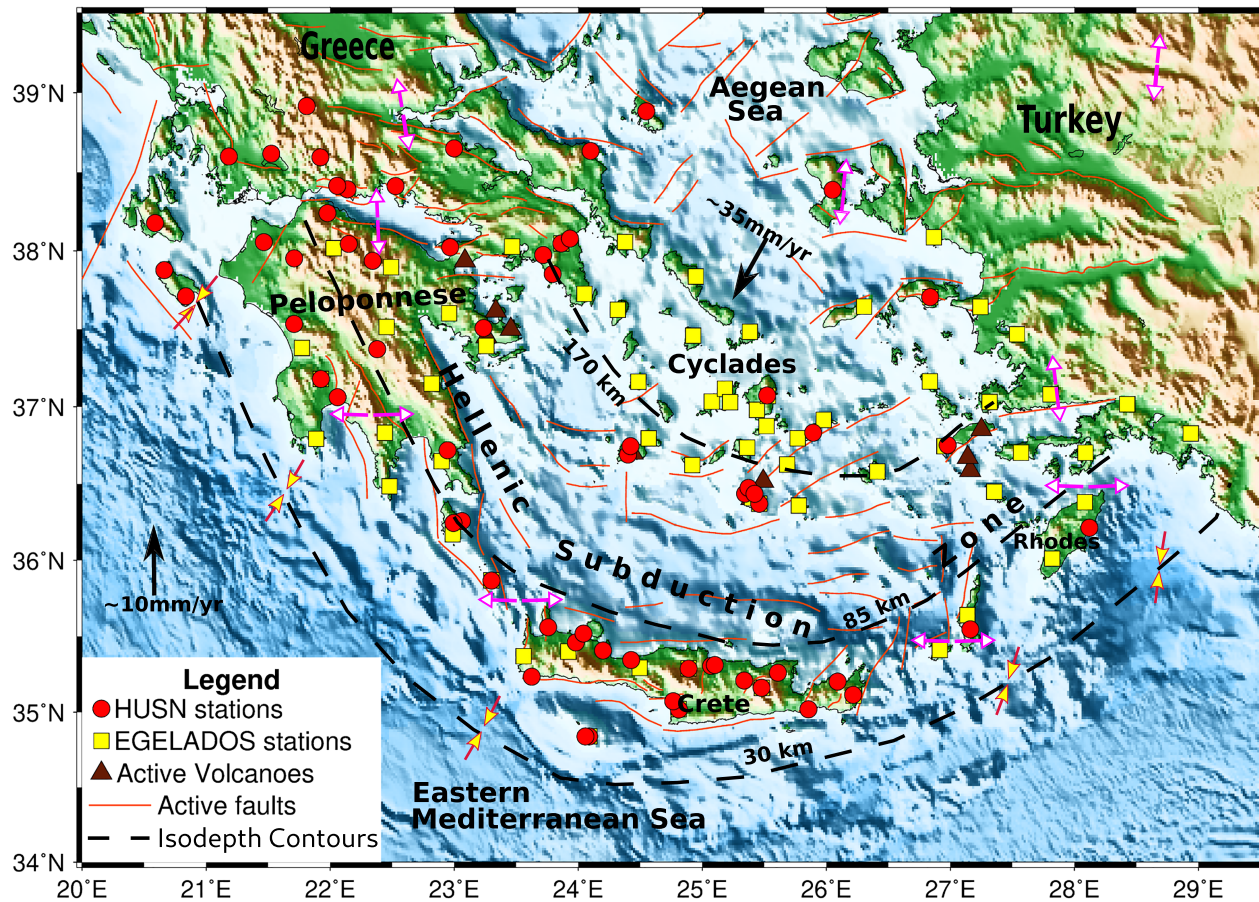
Figure 1. Map representing the topographic and bathymetric features (from ETOPO1: Amante & Eakins, 2009) around the Hellenic Subduction Zone (HSZ) with active faults (from GreDaSS: Caputo et al., 2013), Benioff zone isodepth contours (Papazachos et al., 2000) and active volcanoes. Regional stress field is shown using arrows with white and yellow arrowheads (Konstantinou et al., 2017). Black arrows indicate the southwestward movement of the Aegean microplate at 35 mm/year and northward movement of the Nubian plate at 10 mm/year. The seismic stations used in this study are also depicted. Legend for the symbols used is shown on the bottom left corner of the map.

Knapmeyer, 1999; Meier et al., 2004, 2007; Papazachos et al., 2000; Shaw & Jackson, 2010). The maximum depth of the Wadati-Benioff zone is 160–180 km in the HSZ, much shallower than the downdip extent of the Nubian slab as evidenced from tomographic images (Piromallo & Morelli, 2003; Spakman et al., 1993; van der Meer et al., 2017). This has led to the conclusion that the deeper slab is aseismic (Jackson & McKenzie, 1988; Shaw & Jackson, 2010; Spakman et al., 1988). The sediments scraped off the surface of the downgoing Nubian lithosphere form a thick (up to 10 km) cover south of the Hellenic arc, and they have also partly been accreted in the Aegean crust (Angelier et al., 1982; Foucher et al., 1993; Le Pichon, 1982). Such a complex history of subduction has imparted highly inhomogeneous character to the Aegean lithosphere which is reflected in the seismic waveforms recorded around the HSZ (e.g., Konstantinou & Melis, 2008).

The term inhomogeneity refers to small-scale variations in the propagation medium properties that affect seismic wave amplitudes in the form of scattering loss. Intrinsic loss depends on rock properties and temperature, whereas scattering loss depends on small-scale velocity fluctuations, the presence of microcracks, and partial melting (Sato et al., 2012). The combined effect of these two phenomena is the broadening of seismic wave envelopes. This has been studied extensively by using the Markov approximation of parabolic wave equation, which assumes multiple forward scattering along the ray path, and it is satisfied when the correlation distance of inhomogeneity is much larger than the wavelength of the incident wave (Carcolé & Sato, 2010; Lee & Jokipii, 1975; Saito et al., 2002; Sato, 1989; Sreenivasiah et al., 1976). Scattering strength of a medium can be estimated by measuring the time delay between S wave onset and peak of the S wave envelope,

also called peak delay time (Gusev & Abubakirov, 1999a, 1999b). Peak delay times are insensitive to the intrinsic losses and, therefore, are more reliable for estimating the scattering properties rather than using the entire duration of the S wave envelope (Saito et al., 2002). The peak delay times of S waves have been studied to measure the scattering strength of the propagation medium in Japan, and a strong correlation between the locations of melt and frequency dependence of peak delay times was observed (Obara & Sato, 1995; Takahashi et al., 2007). Small-scale velocity inhomogeneities of varying magnitude are found to be randomly distributed in space (Shiomi et al., 1997). Such random inhomogeneities are modeled using von Kármán-type power spectral density function (PSDF), which has a power law decay in large wave numbers (Saito et al., 2005). Takahashi et al. (2008) derived a recursive formula to estimate peak delay times in a nonuniform von Kármán-type media. They also went on to invert for the von Kármán-type media parameters that describe scattering strength across multiple sections of the Japan subduction zones (Takahashi et al., 2009, 2011, 2013).

The seismic velocity structure of the southern Aegean has been studied using traveltime tomography and receiver functions over the years (e.g., Karagianni et al., 2005; Sodoudi et al., 2006), but to date, there has not been any study to explore the small-scale random inhomogeneities that cause seismic wave scattering. In this paper, we aim to resolve small-scale inhomogeneities in the southern Aegean by inverting the peak delay times of S waves. First, we manually pick the P and S wave arrivals from intermediate depth events recorded by temporary and permanent seismic networks and relocate them using a nonlinear probabilistic location algorithm. Then we calculate the envelopes for each of the associated waveforms in 2- to 4-, 4- to 8-, 8- to 16-, and 16- to 32-Hz frequency bands and measure the peak delay times. After that, we perform a linear regression of peak delay times with hypocentral distance as well as frequency and use the regression parameters to estimate the spatial variation of peak delay time contributions from different depths in all frequency bands. Later, we invert the peak delay times for the parameters of von Kármán-type medium, which model seismic wave scattering. Inversion results indicate zones of high scattering strength in Cyclades, western Crete, and northwest Peloponnese. Regions with high scattering in southwest Cyclades have been shown to exhibit high total Q^{-1} in previous studies suggesting that a major part of total Q^{-1} in this area may come from scattering.

2. Data and Earthquake Locations

In this study, we used seismic waveform data of intermediate depth events, from the temporary EGELADOS (Exploring the Geodynamics of Subducted Lithosphere Using an Amphibian Deployment of Seismographs) network (2005–2007; Friederich & Meier, 2008) and HUSN (Hellenic Unified Seismic Network; early 2011 to March 2018). The EGELADOS network consisted of 57 stations all with broadband three-component (3C) seismometers with 100 Hz sampling rate (f_s). It was complemented by seven stations from GEOFON network operating in the same time period with 3C short period seismometers having 50-Hz f_s including one station from MedNet network with 3C broadband seismometer having 100-Hz f_s. We used all these 65 land-based stations in this study. Apart from these stations, there were also OBS (Ocean Bottom Seismometer) stations in the EGELADOS network, but all of them stopped working soon after installation. Among HUSN stations we used data from 55 stations operating in the southern Aegean, all having 3C broadband seismometers with 100-Hz f_s. Waveforms from events with magnitude $M_L \geq 2$ (according to National Observatory of Athens catalog) recorded by HUSN stations were used because the magnitude of completeness (M_C) for most locations in the southern Aegean is ~2 (D'Alessandro et al., 2011). The station spacing for EGELADOS network is much denser, hence minimum M_C would likely be much less; therefore, all the events recorded by the EGELADOS network were used in this study. The events were first autopicked for P and S arrivals and located, then repicked manually. After final P and S arrivals were obtained, events were relocated with the probabilistic nonlinear location software NonLinLoc (Lomax et al., 2000) using a minimum 1-D velocity model for the southern Aegean (Brüstle, 2012). The RMS residuals (δt) and hypocentral location errors in vertical (δv) and horizontal directions (δh) are shown in Figure S1 of the supporting information. For HUSN data, mean δt is 0.39 s, while mean δv is 7.41 km, and mean δh is 5.15 km. Similarly, for EGELADOS data, mean δt is 0.35 s, while mean δv is 7.53 km, and mean δh is 6.44 km. Only the events with final depths >35 km, RMS residuals <0.5 s, and hypocentral location errors <10 km, in both vertical and horizontal directions, were used in this study. The epicentral locations of all these events along with the ray

paths to the stations that recorded them are shown in Figure 2. It can be seen that the ray coverage is quite good all across the HSZ.

3. Peak Delay Times and Their Characteristics

3.1. Measurement Methodology

In order to measure the peak delay times, we first deconvolved the velocity seismograms from their instrument response at each station. Then we computed the RMS (root-mean-square) of the seismogram amplitudes for two horizontal components (N–S and E–W). This was done to scale up the amplitudes and minimize the inconsistencies in the two components. The seismograms were band-pass filtered into four frequency bands 2–4, 4–8, 8–16, and 16–32 Hz. All seven stations from the GEOFON network in this area have short-period instruments (50-Hz sampling rate); therefore, these were filtered up to the allowed Nyquist frequency, that is, in 2- to 4-, 4- to 8-, and 8- to 16-Hz bands. The envelopes thus obtained were smoothed using the moving average method with window length that is twice the central period in each band (see, e.g., Takahashi et al., 2007). Finally, the time delay from the S wave onset to the peak of the S wave envelope was measured within a 15-s window starting from the S pick and was stored as peak delay time. The time window of 15 s was chosen to exclude surface wave amplitudes or spikes in the signal at later times if any. An illustration of the calculation of peak delay times is shown in Figure 3. After repeating the same set of steps for all waveforms, we obtained 15,353 peak delay times in 2- to 4-Hz band, 15,353 in 4- to 8-Hz band, 15,199 in 8- to 16-Hz band, and 14,690 in 16- to 32-Hz band. We only used the waveforms recorded within 50- to 250-km hypocentral distance range because at larger distances waveforms are influenced by diffraction effects, while at smaller distances the waveforms are affected by source directivity effects. Both of these effects can add bias to peak delay times measurement (Sato, 1989).

3.2. Detrending and Normalization

Peak delay times are expected to increase with hypocentral distance as they are a cumulative effect of repeated scattering. To estimate the trend between peak delay time (t_p) and hypocentral distance (R), we fit the two parameters with a linear relation as follows (Takahashi et al., 2007)

$$\log t_p[f] = C_1[f] + C_2[f]*\log R \tag{1}$$

where C_1 and C_2 are the intercept and slope, respectively. The linear fit obtained for all four frequency bands is plotted in Figure 4 along with the scatterplot of observed peak delay times. The slopes and intercepts obtained from the linear regression are also shown in Figure 4 along with their errors. The errors are an order of magnitude less than the calculated values, therefore acceptable. Although there is a large spread in the peak delay times, we observe a positive slope meaning that there is an increasing trend between peak delay time and hypocentral distance in all four frequency bands. We also measured the variation of peak delay times after removing this increasing trend using the following equation.

$$\Delta\log t_p[f] = \log t_p{}^{\text{obs}}[f] - (C_1[f] + C_2[f]*\log R) \tag{2}$$

The histogram plot of $\Delta\log t_p[f]$ in each frequency band is shown in Figure 5. The histograms are also fitted with a Gaussian curve, shown in red color. The 4- to 8-Hz frequency band has a more peaked distribution compared to other bands and fits well with the normal distribution curve. The 16- to 32-Hz band has the broadest distribution and differs the most from the normal distribution, which indicates that there is a large scatter in $\Delta\log t_p$ in this range. The large scatter in this band could be an indicator of the errors in the identification of S envelope peak. It can be seen from our illustration in Figure 3 that the waveform in 16- to 32-Hz band is contaminated by noise, and the global peak of the envelope barely stands out from the nearby local peaks. Therefore, we conclude that the measurements made in 16- to 32-Hz band may add bias to our peak delay times data set; hence, we exclude this band from further analysis.

Envelope broadening is highly dependent on the frequency content of the seismogram. Higher frequency signals are scattered by inhomogeneities of a smaller scale. Lower-frequency signals, on the other hand, are only influenced by large-scale structure. We follow the approach of Obara and Sato (1995) to find the
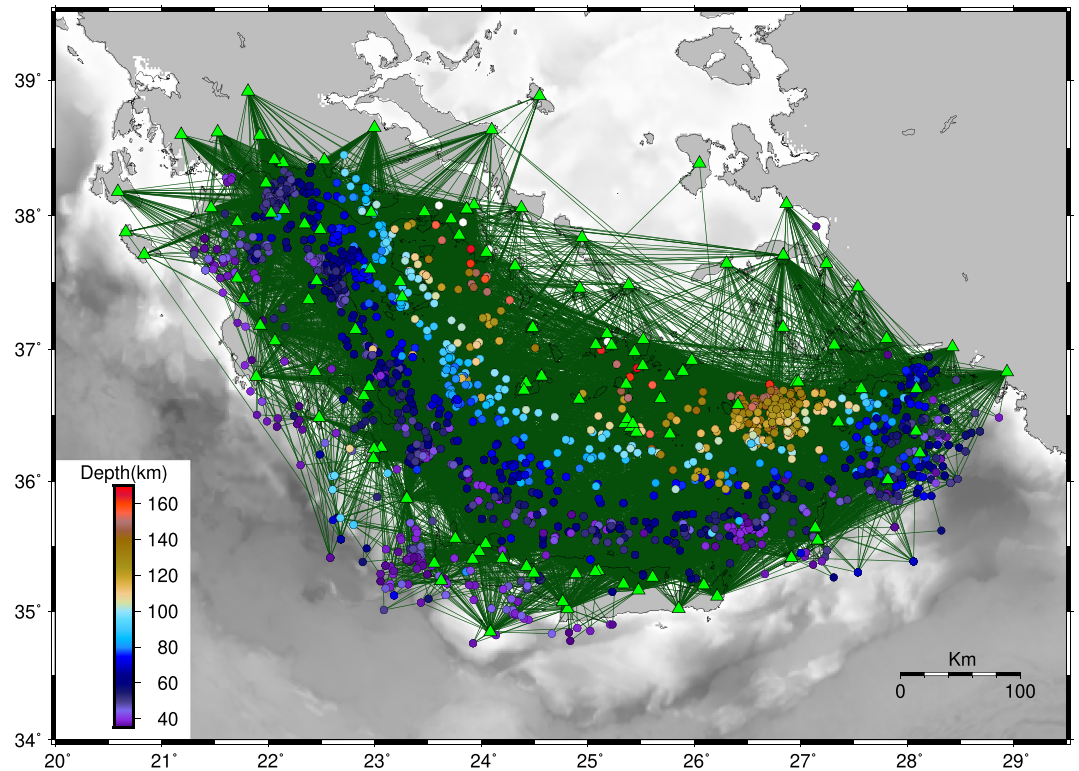
Figure 2. Map showing the ray paths (dark green) from all events (solid circles) to stations (light green triangles) used in this study. The events are color marked as a function of hypocentral depth, as shown in the bottom left corner.

regression relation between peak delay times and frequency for each station. The relation can be expressed mathematically as

$$\log \left(t_p[f \text{ Hz}]/t_p[4\text{–}8 \text{ Hz}]\right) = A_{\text{freq}} + B_{\text{freq}} \log f \tag{3}$$

Peak delay times were normalized by dividing the value in each frequency band with the value in the reference frequency band for each ray, in order to remove the effect of the hypocentral distance dependence on peak delay times. The reference frequency band was chosen to be 4–8 Hz because of the least scatter and the most symmetric distribution of peak delay times in this band as indicated in Figure 5. The B_{freq} parameters obtained from the frequency regression of peak delay times for each station are shown on the map in Figure 6. The stations in the back-arc region show highly positive B_{freq}, which imply larger scattering in higher frequencies and the presence of localized inhomogeneities. Stations such as SANT, ANAF, KIMO, ASTY, KOSI, and TILO, which are closest to the volcanic front show strongly positive B_{freq}. On the forearc side, however, the B_{freq} is much lower (less positive), which could be due to the low scattering path along the slab, taken by rays from deeper events. At some stations in the forearc, B_{freq} is also negative. This could be because high-frequency signals sample small regions of the subsurface along their path, these regions may be more compact than the overall fractured crust in the area and hence cause less scattering. Some stations in the central Peloponnese show positive B_{freq}, which might be influenced by the local structure in the area (faults/cracks).

3.3. Spatial Distribution

In order to study the inhomogeneous properties of the medium, we need to remove the increasing trend of peak delay times with hypocentral distance. Therefore, we calculated $\Delta \log t_p$ from $\log t_p$ using equation (2). Each ray between a source and a receiving station passes through several zones of small to large inhomogeneities, and the $\Delta \log t_p$ we obtain at the receiver is the accumulated delay from each of these zones. The process of delay accumulation is nonlinear, and inversion is required to determine the absolute scattering
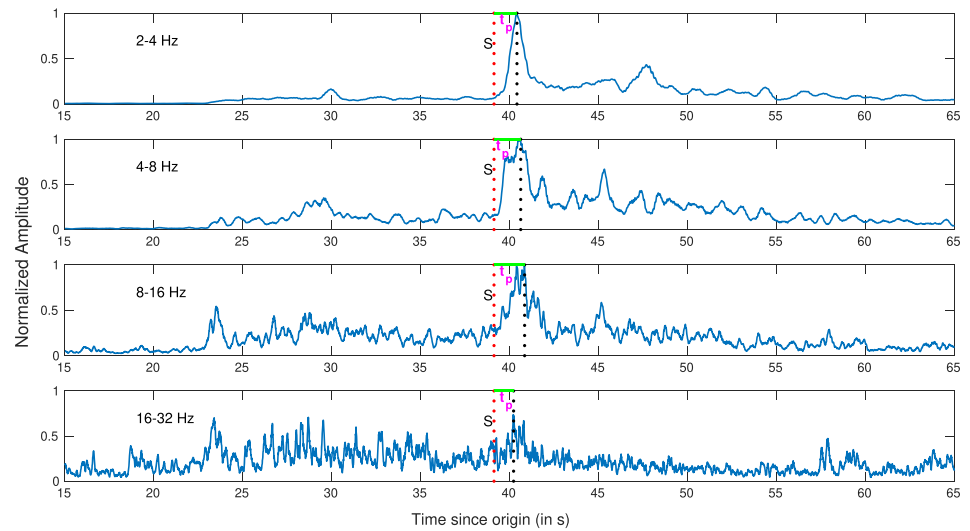
Figure 3. Peak delay time (t_p) calculation for waveforms in 2- to 4-, 4- to 8-, 8- to 16-, and 16- to 32-Hz bands (top to bottom). Envelopes of waveforms are shown in blue color with *S* arrival marked with dotted red line and peak of the envelope marked with dotted black line. Peak delay time is denoted with horizontal green line. The waveform is taken from the 26 June 2011 event (origin time 20:36:51 UTC), which occurred at 38.16°N, 22.08° E and was recorded by ATH station of the HUSN network.

contribution of each zone. However, it is possible to compute the relative scattering contribution without inversion. Considering a single zone of inhomogeneity, there would be multiple ray paths passing through it. Among these ray paths, large $\Delta \log t_p$ are likely a result of accumulation of scattering from inhomogeneities in other zones. Therefore, the minimum value of $\Delta \log t_p$ among these ray paths
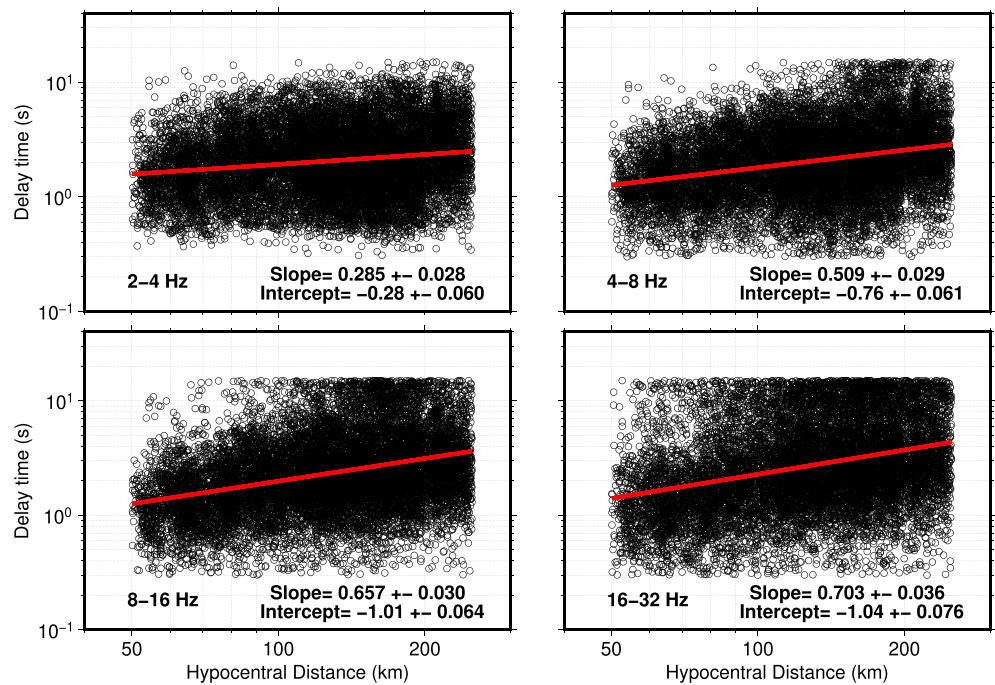

Figure 4. Linear fitting of peak delay time with hypocentral distance in (top left) 2- to 4-Hz, (top right) 4- to 8-Hz, (bottom left) 8- to 16-Hz, and (bottom right) 16- to 32-Hz frequency bands. Red lines indicate the least squares fit. The slope and intercept values of the linear fit are shown in the bottom right corner of each plot along with errors in estimation.
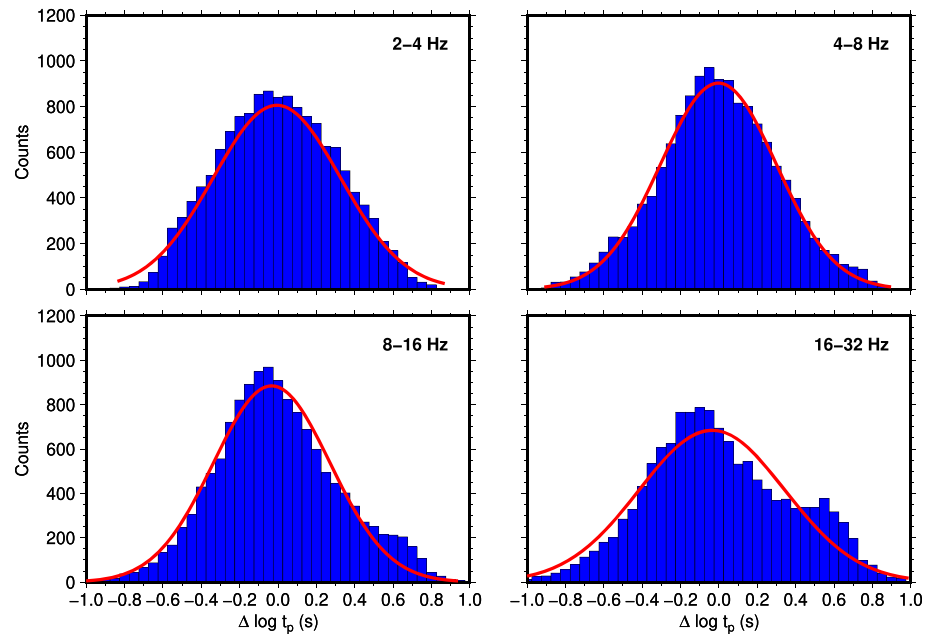
Figure 5. Histogram showing distribution of peak delay times in (top left) 2- to 4-Hz, (top right) 4- to 8-Hz, (bottom left) 8- to 16-Hz, and (bottom right) 16- to 32-Hz frequency bands and Gaussian curves (red) fitting the distributions. The bin size used is 0.05 s in each frequency band.

represents the relative scattering strength of inhomogeneity in the zone (Takahashi et al., 2007). Hence, the minimum-value distribution of $\Delta\log t_p$ from all the zones can give us an idea of relative scattering strength across southern Aegean.

To implement the above method, we divided the whole area into $0.20° \times 0.20° \times$ 20-km grid using nodes at specific locations. Then, we identified the rays that pass through one grid node using Snell's law combined with the nearest neighbor search. Then for each frequency band, the minimum value of $\Delta\log t_p$ among these rays was assigned to the node. This process was repeated for all the nodes to obtain minimum-value distribution of $\Delta\log t_p$ across the nodes in all three frequency bands. Then, smoothing was performed with GMT (Wessel et al., 2013; surface and grdmask command) to obtain the spatial distribution of minimum $\Delta\log t_p$ in southern Aegean as shown in Figure 7. Only nodes with ray coverage of five or more rays are shown, as minimum $\Delta\log t_p$ is not accurate for a smaller number of rays.

We also tested the effect of earthquake location errors on the spatial distribution of $\Delta\log t_p$. We added a random error of up to 10 km in hypocenter depth as well as epicentral location of all the events. Using the events with perturbed locations, we again calculated the $\Delta\log t_p$ for each bin as explained above. The spatial distribution of $\Delta\log t_p$ from perturbed earthquake locations is shown in Figure S2a. The difference in $\Delta\log t_p$ distribution produced by original locations and perturbed locations is shown in Figure S2b. Out of the bins in 0- to 80-km range, 73% of the bins in 2–4 Hz, 74% in 4–8 Hz, and 73% in 8–16 Hz have differences within $\pm$ 0.05 units. As it can also be seen in Figure S2b, the differences in most locations are shown by a light green-blue color representing values close to 0 that are not significant compared to the original $\Delta\log t_p$ values. This shows that the earthquake location errors do not affect the spatial distribution of peak delay times. Therefore, they should not affect inversion results significantly.

The $\Delta\log t_p$ in each frequency band reflects the scattering strength relative to the mean strength in that frequency band. Each frequency band also has a characteristic Fresnel zone or volume. The Fresnel zone defines the volume around the direct ray path that actually influences the properties of waves propagating along the ray and is proportional to the half of the wavelength of the wave when inhomogeneities are small compared to mean medium properties (Červený & Soares, 1992). Therefore, smaller wavelength or higher-frequency waves can sample detailed structures while large wavelength or low-frequency waves can only sample broad variations. At longer delays, the Fresnel volume is larger due to increased scattering.
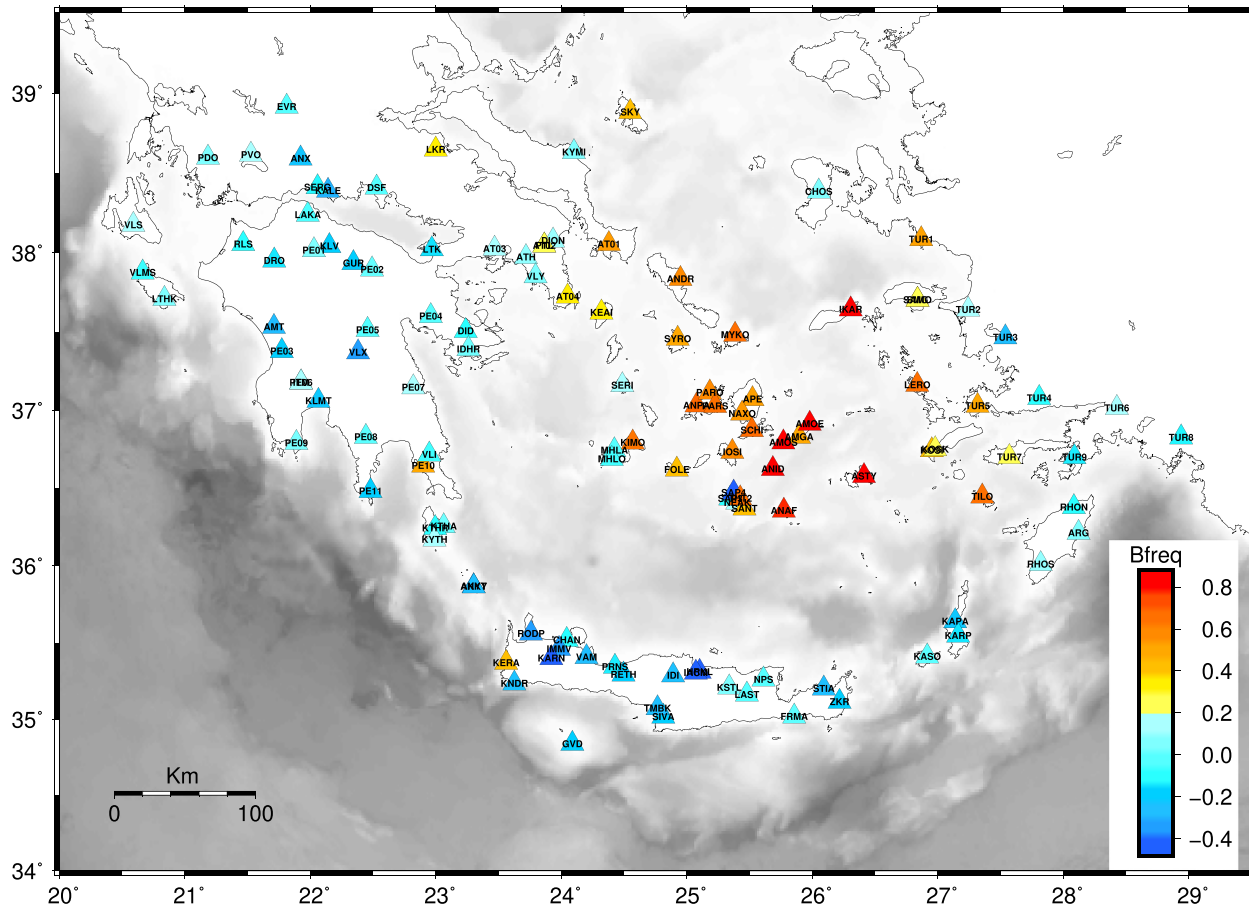
Figure 6. Plot of B_{freq} obtained from the linear fitting of peak delay time with frequency for all the stations. The stations are marked with triangles, color scaled according to their B_{freq} as shown in the bottom right corner.

However, the contribution of delays from inhomogeneities away from the ray path is expected to be small until the peak of the envelope due to small angle scattering (Takahashi et al., 2008). We remove the contributions of these zones largely by subtracting the trend of t_p with hypocentral distance to obtain $\Delta \log t_p$ for each ray path. This trend accounts for the mean delay produced by inhomogeneities across the region. In addition, by assigning the minimum of $\Delta \log t_p$ in each zone, we ensure that larger delays are not taken into account in $\Delta \log t_p$. High $\Delta \log t_p$ is observed in western Crete for 0- to 60-km depth across all frequency bands. This may mean that the inhomogeneous structure beneath western Crete is having varying length scale and is depth invariant. High $\Delta \log t_p$ is also observed in Peloponnese at shallow depths (0–20 km) in all three frequency bands, which also implies scale invariance. Even though most features in the backarc are not apparent from $\Delta \log t_p$ distribution, we observe zones of high $\Delta \log t_p$ in 60- to 80-km range for 8- to 16-Hz band. Subsequently, we invert the peak delay times in order to obtain the spatial distribution of scattering parameters of the medium as discussed in the next section.

4. Inversion for Scattering Parameters

4.1. Background Theory

The small-scale velocity fluctuations in a medium are observed to be randomly distributed in space (Shiomi et al., 1997). If V_o is the average S wave velocity of a medium, the velocity fluctuations can be represented as $V(\mathbf{x}) = V_o \times [1 + \xi(\mathbf{x})]$, where $\xi(\mathbf{x})$ is a random function of space vector $\mathbf{x}$ such that the ensemble average ($<\xi(\mathbf{x})>$) is zero. The inhomogeneous medium is modeled using 3-D isotropic von Kármán-type PSDF as it has power law spectra in large wave numbers compatible with the observations made for velocity inhomogeneities. The PSDF is given as (Sato et al., 2012; Wu & Aki, 1988)
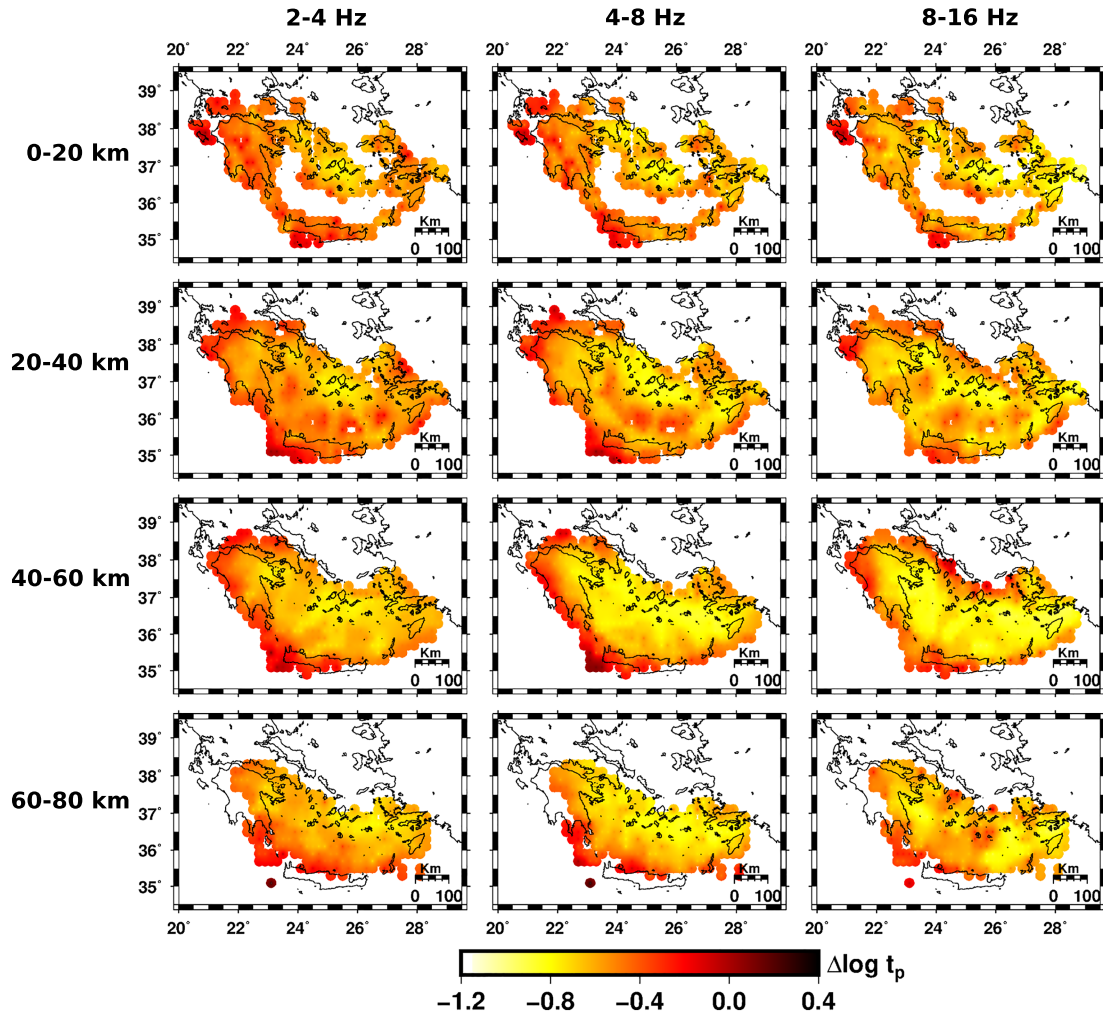
Figure 7. Spatial distribution of Δlog t_p in different frequency bands and depth ranges. Depth increases from top to bottom while frequency increases from left to right.

$$P(m) = \frac{8\pi^{\frac{3}{2}}\varepsilon^2 a^3 \Gamma(\kappa + 3/2)}{\Gamma(\kappa)(1 + a^2 m^2)^{\kappa + 3/2}} \tag{4}$$

where Γ is the gamma function, m is the wave number, ε is the RMS of the fractional fluctuation ξ, "a" is the correlation distance, and κ is a scattering parameter that controls spectral decay in large wave numbers ($am \gg 1$). Using specific values of κ, ε, and a, the random inhomogeneities in the medium can be modeled as a von Kármán type. Parabolic approximation to the elastic wave equation is valid when we neglect large angle scattering, which can be applied to the early part of the S waveform (from the onset to the early coda). The Markov approximation is applied to parabolic wave equation by assuming that the recorded waveform has no contribution from backscattered waves, which is valid for $am \gg 1$. Using these approximations and PSDF of von Kármán-type, the wave equation for an ensemble of wave fields can be solved to model the early part of S wave envelope and related parameters such as peak delay time (t_p) can be calculated (Tatarskii, 1971; Ishimaru, 1978; Sato, 1989; Sato et al., 2012; Saito et al., 2002; Takahashi et al., 2008). Takahashi et al. (2008) developed a recursive formula to calculate peak delay time in nonuniform von Kármán-type media. If we assume n zones ($n \geq 2$) with different κ, ε, and a parameters along a ray, the cumulative peak delay time ($t_p^{(n)}$) observed at the receiving station can be found by recursively calculating the peak delay times across each of these zones. Using the recursive formula, synthetic peak delay times (t_p^{calc}) can be generated for a given number of inhomogeneous zones (n). The scattering parameters that characterize the

inhomogeneous medium are κ and $\varepsilon_{\text{param}} = \log(\varepsilon^{2/(p(\kappa)-1)}a^{-1})$. The $p(\kappa)$ is a numerically estimated function of κ as explained and tabulated in Saito et al. (2002). The parameter κ controls the frequency dependence of peak delay times. Low κ shows greater envelope broadening at higher frequencies. $\varepsilon_{\text{param}}$ controls the amplitude of PSDF at large wave numbers ($m >> 1/a$) in a uniform medium with constant κ and a.

4.2. Inversion Methodology

The study area is divided into blocks of size $0.20° \times 0.20°$ horizontally and 20-km deep with each block having unknown κ and $\varepsilon_{\text{param}}$. These represent the n zones in the recursive formula (Takahashi et al., 2008). The goal of the inversion algorithm is to estimate the κ and $\varepsilon_{\text{param}}$ for each of these blocks. The inversion was performed using the parallel tempering algorithm (Sambridge, 2014) also known as Exchange Monte Carlo method (Hukushima & Nemoto, 1996). This is a variant of random walk Markov Chain Monte Carlo methods. Model parameters (κ and $\varepsilon_{\text{param}}$ in our case) are initialized on multiple chains in parallel, with each chain having a different temperature. Multiple swaps between temperatures of individual chains are allowed probabilistically at each step to prevent the algorithm from being trapped in local minima. Within each chain, the model parameters are randomly perturbed using the Metropolis-Hastings algorithm (Hastings, 1970) at each iteration. The likelihood function that estimates the error at each step in the inversion is given as (modified from Takahashi et al., 2009):

$$E = \sum_{N_{\text{freq}}} \sum_{N_{\text{ray}}(\text{freq})} \frac{\left(t_p^{\text{obs}} - t_p^{\text{calc}}\right)^2}{\sigma_{t_p}^2} + N_{\text{ray}(f_{\text{ref}})} \times w_{B_{\text{freq}}} \times F\left(B_{\text{freq}}, \sigma_{B_{\text{freq}}}\right) + N_{\text{ray}(f_{\text{ref}})} \times [w_k \times L_\kappa + w_\varepsilon \times L_\varepsilon] \tag{5}$$

Here, the first term estimates the error between observed peak delay time (t_p^{obs}) and the modeled peak delay time (t_p^{calc}). The $\sigma_{t_p}^2$ is the standard variance of observed peak delay time, which is assumed to be 0.04 s^2. As the S wave onset was picked manually for each waveform, it is expected that the error in peak delay time measurement should be approximately the standard error in picking ($\sigma = 0.2$ s). This error term is summed over all ray paths in each frequency band ($N_{\text{ray}}(\text{freq})$) and over all three frequency bands ($N_{\text{freq}} = 3$).

The second term contains $N_{\text{ray}(f_{\text{ref}})}$, which is the number of rays in the reference frequency band of 4–8 Hz, and $F\left(B_{\text{freq}}, \sigma_{B_{\text{freq}}}\right)$, which is defined as (Takahashi et al., 2009)

$$F\left(B_{\text{freq}}, \sigma_{B_{\text{freq}}}\right) = \sum_{D=1}^{3} \frac{1}{N_s(D)} \sum_{j=1}^{N_s(D)} \frac{\left(B_{\text{freq}}^{\text{obs}}(j) - B_{\text{freq}}^{\text{calc}}(j)\right)^2}{\sigma_{B_{\text{freq}}}^2(j)} \tag{6}$$

where D is the number of depth ranges for the calculation of B_{freq}, $N_s(D)$ is the number of stations in a particular depth range, $B_{\text{freq}}^{\text{calc}}$ is the B_{freq} obtained for each station using peak delay times generated by the model (t_p^{calc}). $\sigma_{B_{\text{freq}}}^2$ is the variance of error in the estimation of observed B_{freq}. We incorporated the B_{freq} for each station in the inversion to constrain the estimation of κ as it is frequency dependent. We calculated B_{freq} for three hypocentral depth ranges (D) 30–60 km, 60–90 km, and greater than 90 km separately. This was done to constrain B_{freq} at multiple depths as there is a large scatter in peak delay times. Also, the standard error in the estimation of B_{freq} ($\sigma_{B_{\text{freq}}}$) was calculated for all stations at all three depth ranges. The average velocity model for the medium (V_o) was taken as 4 km/s, which is the average of the range of velocity values as seen in tomography results for the southern Aegean (Karagianni et al., 2005).

The third term contains L_κ and L_ε terms which are the Laplacian of κ and $\varepsilon_{\text{param}}$. These terms control the smoothness of the variation of κ and $\varepsilon_{\text{param}}$ in the horizontal plane and also constrain the error at each iteration. Both of them are defined as

$$L_\kappa = \frac{1}{N_{\text{blocks}}} \sum_{\text{blocks}} \left(\nabla^2 \kappa\right)^2 \tag{7}$$

$$L_\varepsilon = \frac{1}{N_{\text{blocks}}} \sum_{\text{blocks}} \left\{\nabla^2 \log\left(\varepsilon^{\frac{2}{p(k)-1}} a^{-1}\right)\right\}^2 \tag{8}$$

Table 1
Initial Constraints on Parameters and Results Obtained After the Inversion

Parameter	Value
Latitude range	33.5° to 39.5°
Longitude range	20.5° to 29.5°
Bin size	0.20° × 0.20° × 20 km
Number of bin nodes	31 × 46 × 5(10, 30, 50, 70, 90 km)
B_{freq} calculation depths	30–60, 60–90, and 90–higher km
$\varepsilon_{\text{param}}$ range	−6.5 to −0.5
κ range	0.1 to 0.9
Uniform initial κ	0.4950
Uniform initial $\varepsilon_{\text{param}}$	−3.3750
σ_{t_p}	0.2 s
σ_{κ}	0.025
σ_{ε}	0.15
Temperature chains	11
Hypo. distance range	50 to 250 km
$w_{B_{\text{freq}}}$	6
$\boldsymbol{w_{\kappa}}$	10
$\boldsymbol{w_{\varepsilon}}$	5
Total iterations	400,000
Burn-in iterations	300,000
RMS error	2.0854 s
RMS error in 2–4 Hz	1.9111 s
RMS error in 4–8 Hz	1.9344 s
RMS error in 8–16 Hz	2.3803 s
$F_{B_{\text{freq}}}$	5.052
L_{ε}	0.4379
L_{κ}	0.0361

where N_{blocks} is the number of blocks in a horizontal plane through which the seismic rays travel in each depth range, ∇^2 represents the Laplacian operator. The smoothing was only applied in the horizontal planes as structure in the vertical direction is expected to be highly variable.

For the inversion process, we used the same set of peak delay time data as used in the regression analysis. The hypocentral distance range (50–250 km) is chosen such that the correlation length a and the wavelength of the wave are much smaller compared to the length of the ray and to get rid of effects such as intrinsic attenuation at large distances. A uniform model was obtained for the region using a grid search approach in the range (0.1, 0.9) for κ and (−6.5, −0.5) for $\varepsilon_{\text{param}}$. These ranges were also chosen as the limits for the perturbation of κ and $\varepsilon_{\text{param}}$ at each iteration in the inversion. The uniform model was found to be 0.4950 for κ and −3.3750 for $\varepsilon_{\text{param}}$. The initial models for 11 Markov chains (on a four core i7 machine) were formed by adding 5% random error to the uniform model in each block. All the 11 chains were assigned temperatures after several trials as follows:

$$T = [1\ 1.3\ 1.69\ 2.10\ 2.86\ 3.71\ 4.83\ 6.27\ 8.16\ 11.29\ 20.33] \qquad (9)$$

Through multiple tests, we realized that the gaps between temperatures should be low at lower levels and should increase with increasing temperatures for greater mixing and faster convergence. At each iteration, one of the model parameters (κ or $\varepsilon_{\text{param}}$) in one of the blocks ($N_{\text{blocks}}$) was perturbed by drawing from a normal distribution around its value with standard deviation 0.025 for κ (σ_{κ}) and 0.15 for $\varepsilon_{\text{param}}$ (σ_{ε}). The models were accepted or rejected based on the likelihood function value from equation (6) at each iteration (Hastings, 1970). The three weighting parameters were determined through multiple trial runs as $w_k = 10$, $w_{\varepsilon} = 5$, and $w_{B_{\text{freq}}} = 6$.

The algorithm was first run for 200,000 iterations to perform multiple tests. The likelihood probability and RMS error in peak delay times were monitored regularly, and the number of burn-in steps (steps needed for inversion to reach a stable posterior distribution) were set as 150,000 in each of these tests. Finally, the algorithm was run for 400,000 iterations with the chosen value of weighting parameters and burn-in steps were set to 300,000. After the burn-in steps, the results at each iteration were saved for the highest temperature chain and the final model was obtained by averaging them. The initial constraints on the parameters used in the inversion, the RMS error between t_p^{obs} and t_p^{calc} obtained using inverted κ and $\varepsilon_{\text{param}}$, and the values of B_{freq} estimation function ($F_{B_{\text{freq}}}$) and smoothing parameters (L_{ε} and L_{κ}) are listed in Table 1. The final results for κ and $\varepsilon_{\text{param}}$ are mapped in Figures 8 and 9, respectively, for 0- to 80-km depth range.

4.3. Description of Inversion Results

Strong inhomogeneous regions with low κ are observed across the southern Aegean (Figure 8). At shallow depths (0–20 km), low κ is observed in Cyclades and Peloponnese. As we go deeper, low κ regions become more and more restricted to the back-arc area. Anomalously low κ is observed along western and southern fringes of the HSZ at larger depths (40–60 and 60–80 km). This may be due to poor ray sampling in these bins. On the other hand, $\varepsilon_{\text{param}}$ is high across Peloponnese, Crete, and Rhodes in 0- to 20-km range (Figure 9). In Cyclades, $\varepsilon_{\text{param}}$ is low in the backarc but medium to high below the volcanic front for 0- to 20-km range. As we go deeper, zones with high $\varepsilon_{\text{param}}$ gradually shift to low values and vice versa. Independent values of ε and a are required as input to equation (4), in order to calculate the PSDF (P(m)). Numerical modeling by Takahashi et al. (2008) showed that changing the correlation distance of inhomogeneity (a) has negligible effect on the P(m) at large m or high f. However, at small m or low f, a significant shift in the value of P(m) is seen with small change in a. Therefore, P(m) calculated from κ and $\varepsilon_{\text{param}}$ can safely represent the scattering strength of inhomogeneities at large m, even using a constant value of a such that $am \gg 1$. Using $a = 5$ km, large wave number criterion implies $m \gg 0.2$ km^{-1}. Therefore, $m = 15$ km^{-1} is a reasonable value
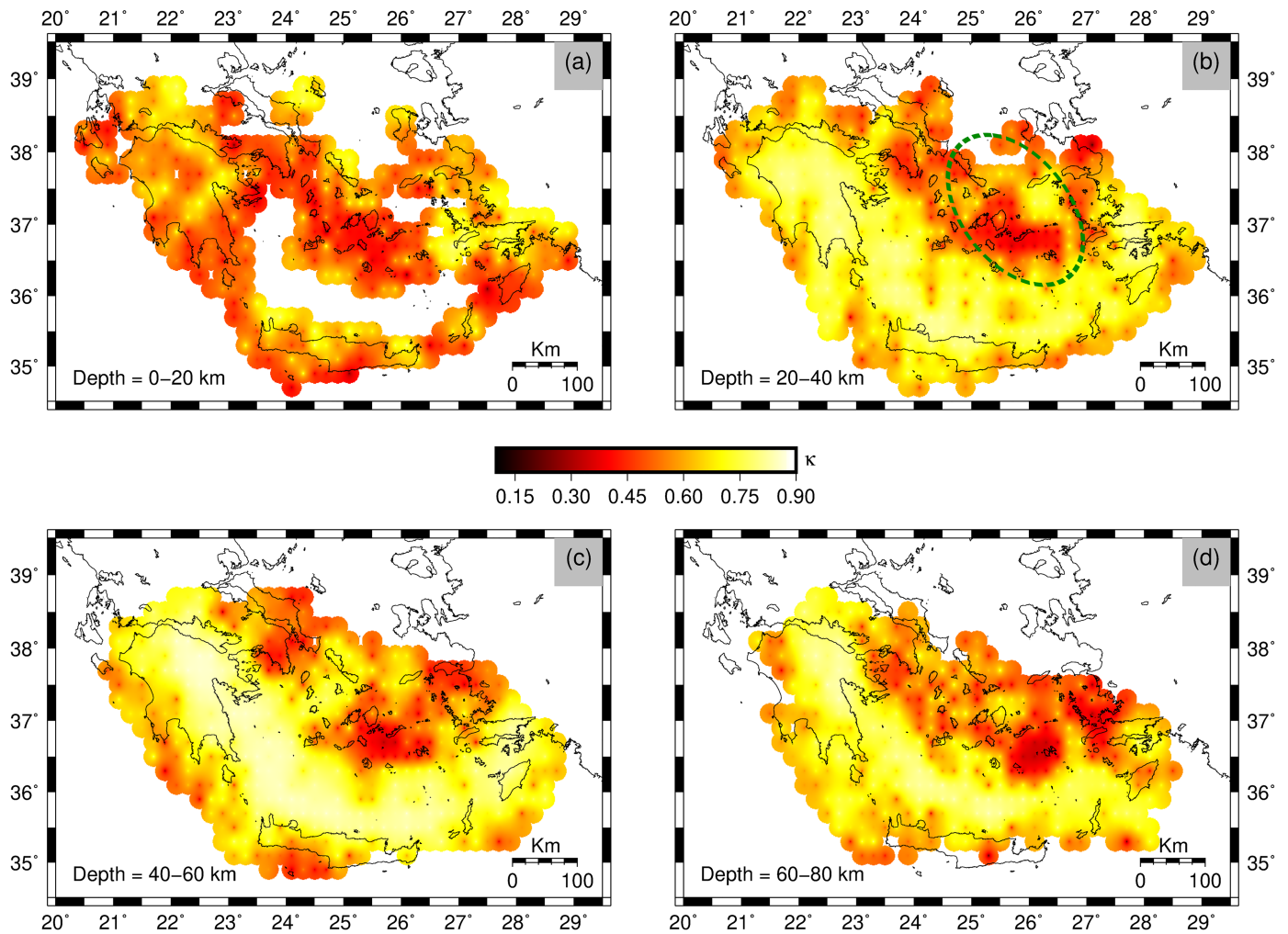
Figure 8. Spatial variation of κ obtained after inversion for 0- to 20-km, 20- to 40-km, 40- to 60-km, and 60- to 80-km depth ranges as shown in (a)–(d), respectively (see text for more details). A dashed green curve in the 20- to 40-km section indicates the low-velocity zone in the mantle wedge (Karagianni et al., 2005).

fitting this criterion and implies a frequency of 10 Hz with $V_o = 4$ km/s. As the scattering of seismic waves is mainly caused by inhomogeneities having a scale larger than the wavelength of incident wave, $P(m_l)$ [$P(m = 15 \text{ km}^{-1})$] represents the scattering strength of inhomogeneities for frequencies higher than 10 Hz. At shallow depths, the pattern of $P(m_l)$ is quite similar to the pattern of $\varepsilon_{\text{param}}$. However, we see the effect of low κ (more than $\varepsilon_{\text{param}}$) on $P(m_l)$ in larger depths where very high values are observed in the back-arc region (Figure 10).

4.4. Sensitivity Tests

We performed four types of sensitivity tests, namely odd-even data set test, weighting parameters sensitivity test, velocity sensitivity test, and window length test as explained below. The inversion algorithm was run for 200,000 iterations in each of these tests. The final RMS error in the inversion as well as $F_{B_{\text{freq}}}$, L_κ and L_ε values are given in Table S1 of the supporting information for all the tests.

In order to check the stability of our results, we performed separate inversions on two subsets of our data. The subsets were obtained by numbering all the events used in this study and forming separate data sets from waveforms of even- and odd-numbered events. The results obtained after inversion are shown in Figures S3 and S4. As we can see, there are no significant differences between the inversion results of odd and even data sets and both results are quite close to our final inversion result using all the waveforms at once (Figure S5).
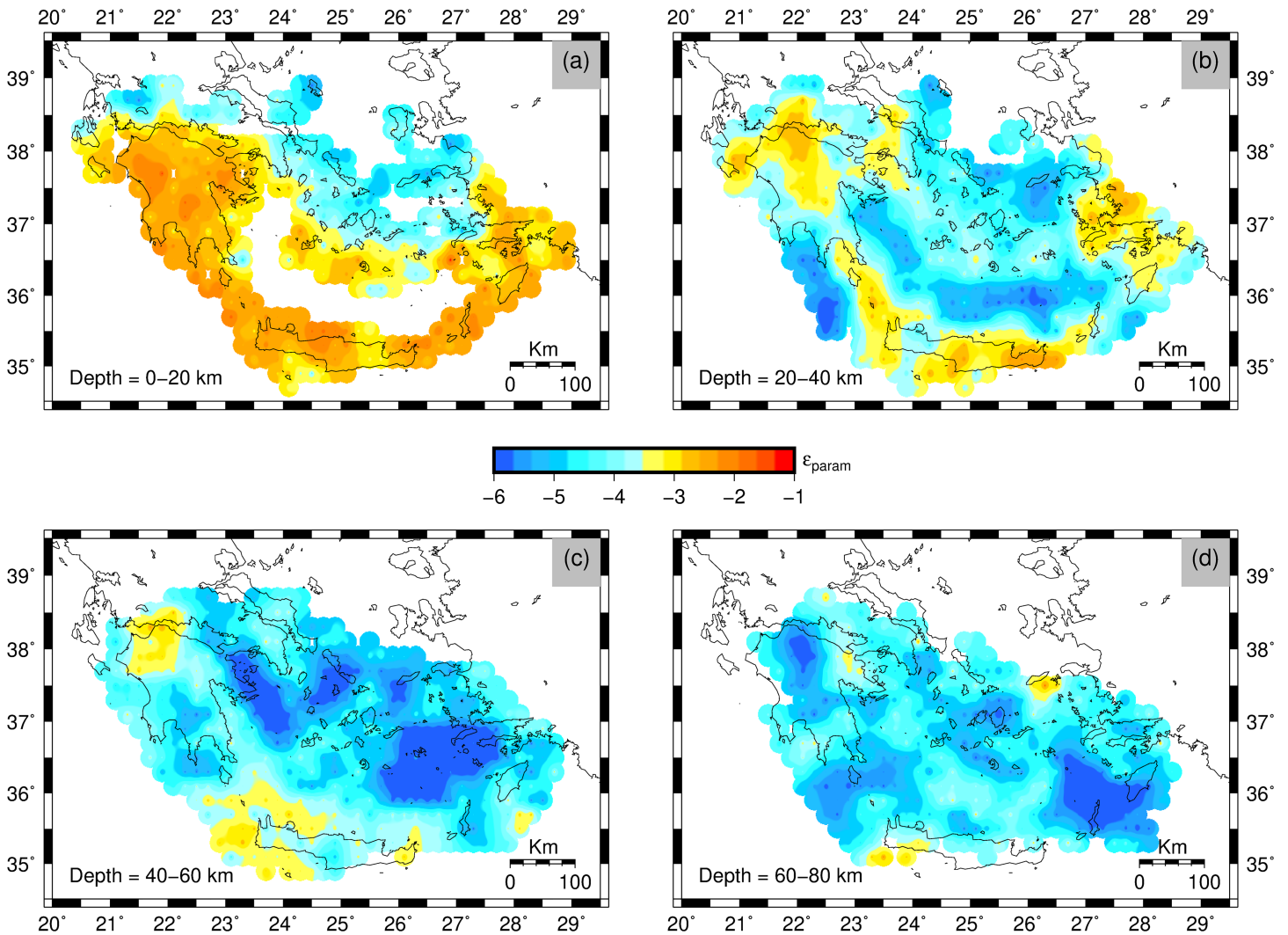
Figure 9. Spatial variation of $\varepsilon_{\text{param}}$ in (a) 0- to 20-km, (b) 20- to 40-km, (c) 40- to 60-km, and (d) 60- to 80-km depth range after inversion (see text for more details).

The results of odd data set show less RMS value and less error in B_{freq} estimation compared to the even data set (Table S1) but this small variation is expected as the data set division is pseudorandom. This test shows that the systemic errors in the data set are small and inversion results are stable.

There are three weighting parameters in the inversion algorithm: w_k, w_ε, and $w_{B_{\text{freq}}}$. We tested the sensitivity of each of these parameters one by one. For the first test, we increased w_k from 10 to 50 while keeping $w_\varepsilon = 5$ and $w_{B_{\text{freq}}} = 6$. The results obtained for κ and $\varepsilon_{\text{param}}$ are shown in Figure S6. There are not many observable differences in these results when compared to the results obtained using the original parameters. In the next stage, we kept w_k and $w_{B_{\text{freq}}}$ same as the original while increased w_ε from 5 to 10. The results obtained after inversion are shown in Figure S7. Again, there are minimal differences from the original result (Figure S5). Even though the inversion results for higher values of weighting parameters for κ and $\varepsilon_{\text{param}}$ are more smoothed, the overall RMS error and the RMS error in individual frequency bands are higher than the original inversion result (Table S1). We also compared the results with high $w_{B_{\text{freq}}}(10)$ and low $w_{B_{\text{freq}}}(3)$ as shown in Figures S8 and S9, respectively. Again, there are no striking differences from the original κ and $\varepsilon_{\text{param}}$ inversion results (Figure S5). Results with high $w_{B_{\text{freq}}}(10)$ are having slightly less RMS error and B_{freq} estimation error compared to the inversion results based on chosen parameters but the results are less smooth as indicated by smoothing parameter values (L_κ and L_ε; Table S1). Thus, from these sensitivity tests, we conclude that the weights used in our inversion mostly control the rate of convergence of the algorithm, provided that they are not too high or too low.

We also tested the sensitivity of our final results to changes in average medium velocity (V_o). The average V_o in the HSZ is 3.6 km/s in the crust, while the average V_o is 4.4 km/s in the Aegean uppermost mantle (Karagianni et al., 2005). We separately inverted with 3.6 and 4.4 km/s as V_o for κ and ε_{param}. The results obtained for lower V_o (3.6 km/s) are shown in Figure S10, while those for higher V_o (4.4 km/s) are shown in Figure S11. There are no significant differences in κ except in the 20- to 40-km depth range. Even at this depth, broad features are the same. The differences are mainly a result of the variable degree of smoothness achieved in the two results and will likely improve with more iterations. For ε_{param} results, however, there is a shift toward lower values for low V_o (Figure S10) and higher values for high V_o (Figure S11), even though the pattern of variation is similar to that of the results with original V_o. Such a shift is expected, as ε_{param} accounts for the velocity perturbation from the average (ε) along with the term for the correlation distance of inhomogeneity (a). Since in this test we only change the average medium velocity, ε_{param} shifts according to the amount of the velocity change.

Finally, we tested the effect of window length on the inversion results. We calculated peak delay times in four different time windows, namely 15, 20, 25, and 30 s from the onset of S pick. We separately inverted each of the four time window data sets for κ and ε_{param} keeping all other inversion parameters the same. The results obtained after inversion are shown in Figures S5 and S12–S14 for 15, 20, 25, and 30 s, respectively. Even though there are no significant differences in the results for the four time windows, the errors after the inversion become larger with the increasing window length (Table S1). The forward model used in the inversion is based on the parabolic approximation to the elastic wave equation which is only valid for the early part of the wave envelope. This is because parabolic approximation assumes small angle scattering (Saito et al., 2002). As we increase the window length, the increase in peak delay time may be caused by refocusing of energy from large-angle scattering, which negates the basic assumption of parabolic wave equation. Therefore, the predicted peak delay times are smaller than the peak delay times measured in case of larger window length. Hence, we conclude that the window of 15 s is the most suitable window length for peak delay time analysis as well as inversion, since it has the least error (Table S1).

5. Discussion

The spatial distribution of κ and ε_{param} depends on the nature of interaction of inhomogeneities with large wave number (m) or high-frequency (f) S waves. κ solely controls the frequency dependence of inhomogeneities. Low κ indicates high scattering in high frequencies. ε_{param} ($\log(\varepsilon^{2/(p(\kappa)-1)}a^{-1})$) controls the amplitude of PSDF ($P(m)$) in large wave numbers for a constant κ medium. Higher ε_{param} implies higher scattering strength of inhomogeneity at constant κ. $P(m_l)$ [$P(m = 15 \text{ km}^{-1})$] with $a = 5$ km combines the effect of κ and ε_{param} and represents the scattering strength of inhomogeneity in frequencies higher than 10 Hz (using $V_o = 4$ km/s). Strong inhomogeneities may be produced by a variety of sources including fluids of hydrothermal/magmatic type, deformed crustal layers, intrusion of different rock types, and randomly oriented cracks/fractures (Takahashi et al., 2013). As a consequence, some of the results from tomography studies will be correlated with our inversion results in the HSZ. However, the regions which show strong scattering may not necessarily exhibit large velocity contrasts. Therefore, we should not expect a one to one correlation of velocity anomalies with the results of this study.

Peloponnese marks the western boundary of the HSZ. Crustal thickness across this region varies from 25 to 36 km, with the least thickness observed in the northwest (NW) part, while the maximum thickness is observed in the central part (Sodoudi et al., 2006). Different sections of Peloponnese have been studied using traveltime tomography, seismic reflection surveys, and other imaging techniques (e.g., Halpaap et al., 2018; Suckale et al., 2009; Underhill, 1988). Traveltime tomography performed using P and S waves in the western HSZ shows very high V_p/V_s (1.85–1.95) for NW Peloponnese at 15-km depth (Halpaap et al., 2018). We observe a zone of very high ε_{param} and low κ with high $P(m_l)$ for this area in 0- to 20-km depth (Figure 8a). These results along with very high V_p/V_s point toward the presence of fluids. There are evidences of mantle fluids in this region based on elevated pore-fluid pressure in fault zones which are misoriented with respect to the maximum regional stress axes (Konstantinou et al., 2011). These mantle fluids have also been evidenced from the presence of mantle-derived Helium isotope ratio in spring waters in the same area (Pik & Marty, 2009). Besides, seismic reflection surveys along the western Greece continental margin reveal the presence of salt diapirs intruding through the sediment cover (Brooks & Ferentinos, 1984; Melis &
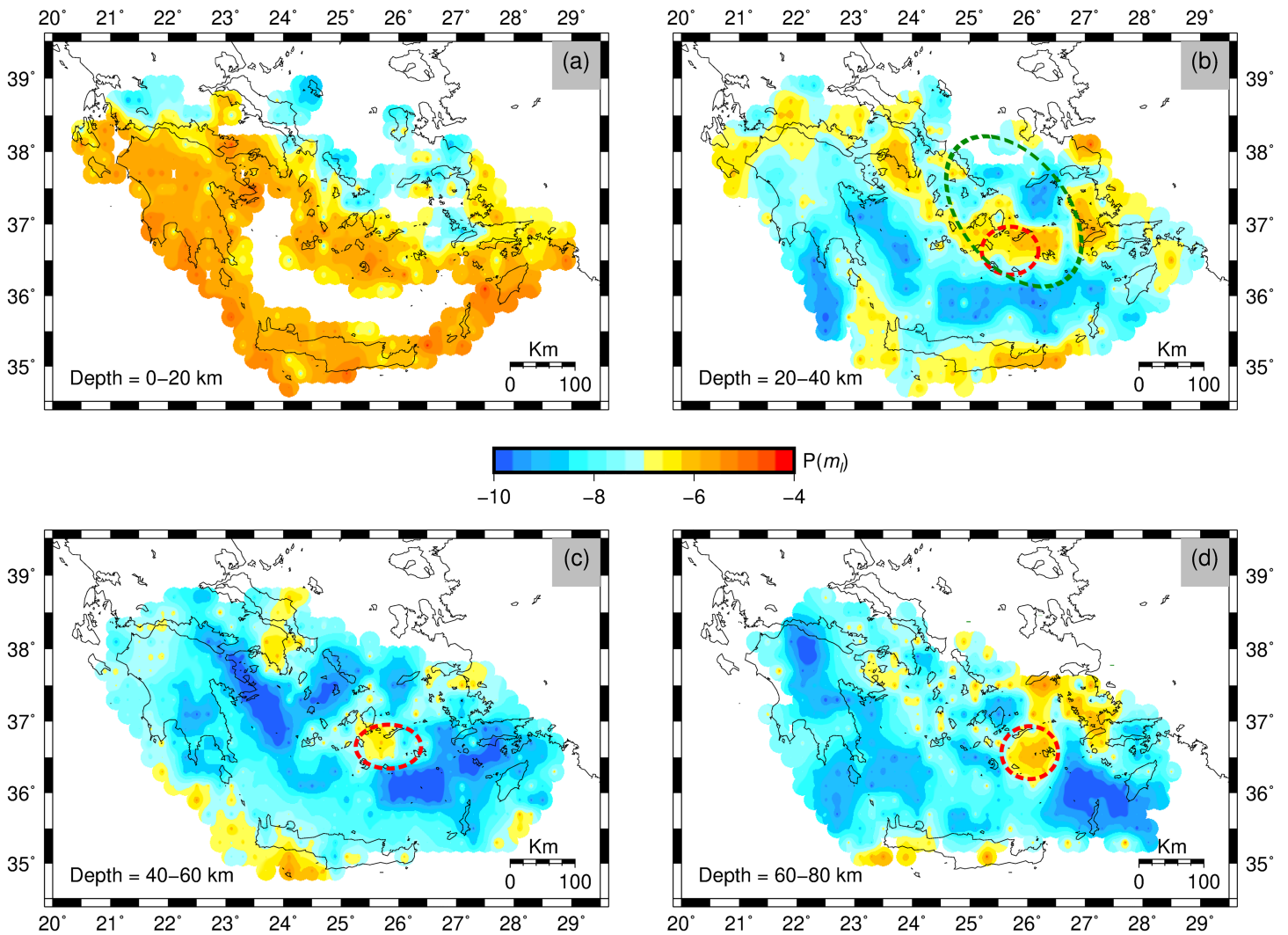
Figure 10. Spatial variation of PSDF $P(m_l)$ (P(m) at $m = 15$ km^{-1}) in (a) 0- to 20-km, (b) 20- to 40-km, (c) 40- to 60-km, and (d) 60- to 80-km depth ranges obtained by using final κ and ε_{param} from inversion (see text for more details). Dashed red curves in the 20- to 40-km, 40- to 60-km, and 60- to 80-km sections indicate the region with high Q_s^{-1} (0.0025–0.004 units) in eastern Cyclades (Ventouzi et al., 2018). A dashed green curve in the 20- to 40-km section indicates the low-velocity zone in the mantle wedge (Karagianni et al., 2005).

Tselentis, 1998; Underhill, 1988). Salt diapirs have sharp geometry and are known to cause diffraction of seismic waves (e.g., Jones & Davison, 2014). These structures have dimensions of the order of a few kilometers and should be well-sampled using high-frequency bands (4–8 and 8–16 Hz). Therefore, such structures, if present below the NW margin of Peloponnese, would likely contribute to the strong inhomogeneities. We also see high $P(m_l)$ across other sections of Peloponnese in 0- to 20-km depth while tomography results show close to average V_p/V_s for these sections (Halpaap et al., 2018). High-resolution images of velocity perturbation from the inversion of teleseismic scattered waves indicate a stack of alternating anomaly in western Peloponnese that appears to detach from the subducting slab at depths shallower than 20 km (Pearce et al., 2012; Suckale et al., 2009). This anomaly stack is interpreted as upper crustal layers consisting of sedimentary rocks and crystalline oceanic basement scraped off the subducting oceanic lithosphere and thrust on to the continental lithosphere in different structural levels since the Eocene (Neumann & Zacher, 2004; Suckale et al., 2009). Such deformation of continental crust in multiple stages would not produce large-scale velocity contrasts to be detected in tomography results. However, it may generate strong inhomogeneities with clear frequency dependence indicated as high ε_{param} and low κ across Peloponnese in 0- to 20-km depth (Figures 8a and 9a). A similar anomaly with high ε_{param} and low κ have been observed in Sendai plains of Japan, which was interpreted as resulting from reverberation in

sediment layers (Takahashi et al., 2009). Tomography results also show lower than average V_p/V_s (1.68–1.70) at 30- and 40-km depths for central Peloponnese (Halpaap et al., 2018). Low V_p/V_s in the lower crust has been interpreted by Halpaap et al. (2018) as a zone of silica enrichment from sediment-derived fluid migration, also proposed for Cascadia (Hyndman et al., 2015) and observed in exhumed outcrops in New Zealand (Breeding & Ague, 2002). Our results show small inhomogeneities with moderate to low P (m_l) resulting from moderate ε_{param} and high κ in 20- to 40-km range (Figure 10b). For depths 50, 65, and 80 km, close to average V_p/V_s (1.73–1.76) is indicated in tomography results over most of Peloponnese. At these depths, a dry mantle wedge corner along with a sealed plate interface have been proposed to explain the close to average V_p/V_s (Halpaap et al., 2018). Such features also point toward the absence of inhomogeneities which is consistent with our observations of low P (m_l) along with high κ and low ε_{param} in 40- to 80-km depth (Figures 8c, 8d, 9c. 9d, 10c, and 10d).

To the south, Crete island has been studied extensively using seismicity, receiver functions, surface wave dispersion, and geochemical studies. Teleseismic receiver functions complemented with Rayleigh wave dispersion studies reveal both the Aegean continental Moho (35 km deep) and the African oceanic Moho (55 km deep) in central Crete, while only African oceanic Moho in western Crete (Endrun et al., 2004). This implies lateral inhomogeneity in the crust of Crete from the western to the central part. Paleoshorelines in coastal Crete indicate massive uplift of this area, up to 23 m above sea level (Pirazzoli et al., 1982; Gallen et al., 2014; Strobl et al., 2014; Tiberti et al., 2015; Mouslopoulou et al., 2015). This uplift has been attributed to sediment underplating (Angelier et al., 1982; Gallen et al., 2014), updip flow of serpentinized rocks through a subduction channel (Endrun et al., 2004; Meier et al., 2007), isostatic adjustment to the mass deficit of Aegean lithosphere (Snopek et al., 2007), and one or more megathrust earthquakes (Mouslopoulou et al., 2015; Shaw et al., 2008). As a result of uplift, Crete forms a horst structure with graben on its either side. Our inversion results show moderate P (m_l) with moderate to high ε_{param} in 0- to 60-km depth across Crete (Figures 8a–8c and 9a–9c). In 20- to 40-km depth, high P (m_l) is observed in western Crete while low P (m_l) is seen in central Crete (Figure 9b). This may be due to lateral inhomogeneity in the lower crust of Crete. Inhomogeneities in 0- to 60-km depths is possibly generated by one or more sources that cause the uplift. Moderate P (m_l) south of Crete in 40- to 60-km depth could be due to material underplating of the Aegean crust by sediments derived from the slab (Gallen et al., 2014). Receiver function studies also show a negative anomaly in these depths, which has been interpreted as underthrusting of sediments scraped off the subducting slab (e.g., Knapmeyer & Harjes, 2000). Sediments are known to scatter seismic waves near the surface (e.g., Boore et al., 1971). At the Moho boundary, sharper velocity contrasts of these sediment bodies would likely generate strong inhomogeneities. Updip flow of serpentinized material through the horst and graben structure (Meier et al., 2007) may contribute to inhomogeneities observed underneath Crete in 20- to 40-km depth and south of Crete in 40- to 60-km depth. Crete has a history of large thrust earthquakes as indicated by the study of the relation between altitude of paleoshorelines and their radiocarbon ages. These earthquakes have also contributed to the uplift of Crete episodically (Mouslopoulou, Nicol, et al., 2015). Such large thrust earthquakes can cause considerable deformation in the overriding Aegean crust, which may also generate inhomogeneities in the form of high to moderate ε_{param} observed in 0- to 40-km depth range. A similar anomaly with moderate ε_{param} and moderately low κ was observed in east off Aomori region of Japan, which is located near the rupture area of 1968 Tokachi-oki earthquake (M 8.2; Takahashi et al., 2009).

The Cyclades constitute the volcanic and the back-arc regions of the HSZ. Karagianni et al. (2005) used group velocities of Rayleigh wave fundamental mode to derive S wave velocity structure for the Aegean crust and uppermost mantle. They observed crustal S wave velocities (~3.5 km/s) in 0- to 20-km depth and upper mantle velocities (4.2–4.4 km/s) in 20- to 30-km depth across Cyclades. We observe zones of low κ in 0- to 40-km depth for most of Cyclades (Figures 9a and 9b). This region coincides with the aerial extent of MCC. MCCs were formed as a result of exhumation of high-pressure, low-temperature metamorphosed middle to lower crustal rocks along ductile shear zones due to extension in the Aegean crust (Tirel et al., 2008). Even though there are no quantitative studies about the inhomogeneity in metamorphic bodies, we speculate that such a complex process of exhumation can generate inhomogeneities that scatter the high-frequency waves more and, therefore, produce low κ (Figures 8a and 8b). In 30- to 40-km depth, a low-velocity zone has also been observed in the back-arc region (dashed green curve in Figure 10b). These depths have been associated with the mantle wedge fluid activity as the Moho depth is <30 km in Cyclades (Karagianni et al., 2005; Sodoudi et

al., 2006). Release of fluids in the mantle wedge would likely contribute to the scattering with zones of low κ and moderate to high $P(m_l)$ in 20- to 40-km range (Figures 8b and 10b). Cyclades also marks the region where subducting Nubian lithosphere reaches depths of more than 100 km. Models for pressure-temperature paths of mineralogical transitions and seismic wave dispersion studies from deep earthquakes show that hydrous phases are present in the subducting slab at depths greater than 100 km even up to 250 km (Abers, 2000; Peacock, 1993). At such depths, slab dehydration releases extensive amount of fluids which enter the mantle wedge and produce partial melts as they reach appropriate pressure-temperature conditions. The partial melts being lighter migrate upward and get collected in a large magma reservoir (Papazachos et al., 2005). Tomography studies indicate the depth of this magma reservoir to be around 60–90 km in the HSZ (Papazachos et al., 1995). Our results also show very low κ in patches all across the back-arc region in 60- to 80-km depth, which indicates that the high inhomogeneity of this zone is clearly linked to the main magma reservoir in the upper mantle (Figure 8d).

Inhomogeneities described by κ and ε_{param} reflect the medium properties that cause scattering attenuation of S waves and can be correlated with quality factor (Q^{-1}) estimates. Recently, Ventouzi et al. (2018) calculated the total S wave quality factor (Q_s^{-1}) for southern Aegean in different depth sections using the events recorded by EGELADOS and HUSN networks (similar to our study). The authors used a 5-s window after the S pick to calculate the frequency spectrum of the signal and measured the slope of the spectrum from maximum corner frequency to the point where signal to noise ratio drops to 3. This slope is directly proportional to Q_s^{-1}. Highest Q_s^{-1} in the back-arc region has been found in 60- to 80-km depth, in agreement with high $P(m_l)$ and very low κ for eastern Cyclades in the current study (Figure 8d). Also, Peloponnese shows low $P(m_l)$ in 20- to 80-km depth consistent with low Q_s^{-1} observed at these depths. In 20- to 80-km depth sections, very high Q_s^{-1} is observed in eastern Cyclades. Our results also show high $P(m_l)$ for eastern Cyclades in this depth range (Figures 10b–10d, dashed red curves). This implies that a significant part of the S wave attenuation in 20- to 80-km depths for eastern Cyclades may be due to scattering losses.

6. Conclusions

We used 1,718 manually picked and relocated events with hypocentral depths more than 35 km to measure S wave peak-delay times (t_p) and inverted them in order to calculate parameters that describe the spectral characteristics of inhomogeneity in the southern Aegean. This study is the first attempt to resolve the distribution of random inhomogeneities in the HSZ. The main conclusions of the present work are summarized below:

i   Very high $\Delta \log t_p$ is observed in western Crete in 0- to 60-km depth for all frequencies, and high $\Delta \log t_p$ is observed in Peloponnese for all frequencies at shallow depth. This indicates frequency independent scattering in western Crete and Peloponnese. Such a dependence implies that the inhomogeneities in Peloponnese and Crete are of varying scale.

ii High $P(m_l)$ [$P(m = 15 \text{ km}^{-1})$] with low κ is observed across Peloponnese for shallow depths (0–20 km) implying strong inhomogeneities. Such values are likely a result of intermixing of oceanic upper crust with continental crust and subsequent deformation at multiple levels. Very high ε_{param} and low κ in north-west Peloponnese may be related to rising mantle fluids and salt diapirs. Moderate to low $P(m_l)$ is observed in 20- to 40-km depth for Peloponnese. This implies low level of scattering in the silica enrichment zone in the lower crust.

iii Moderate $P(m_l)$ with high to moderate ε_{param} is observed across Crete in 0- to 60-km depth. It may be the result of a combination of different factors. Inhomogeneities in 0- to 40-km range may be due to a history of large thrust earthquakes in the area while inhomogeneities in 40- to 60-km range could be related to sediment underplating as well as the backward flow of metamorphosed rocks through a subduction channel.

iv Zones of low κ in Cyclades for 0- to 40-km depth are closely associated with the location of MCCs which may produce inhomogeneities due to their complex exhumation process. Very low κ and high $P(m_l)$ in 60- to 80-km depth is closely associated with the location of the main magma reservoir beneath the back-arc region. This feature is also observed in the velocity and attenuation tomography studies in the HSZ.

v $P(m_l)$ in Peloponnese and Cyclades shows good correlation with previous S wave attenuation (Q_s^{-1}) results. A significant portion of high Q_s^{-1} in eastern Cyclades which exhibits high $P(m_l)$ for 20- to 80-km depth may be due to scattering losses.

References

Abers, G. A. (2000). Hydrated subducted crust at 100–250 km depth. *Earth and Planetary Science Letters*, *176*(3–4), 323–330. https://doi.org/10.1016/S0012-821X(00)00007-8

Amante, C. and B.W. Eakins, 2009. ETOPO1 1 arc-minute global relief model: Procedures, data sources and analysis. NOAA Technical Memorandum NESDIS NGDC-24. National Geophysical Data Center, NOAA. https://doi.org/10.7289/V5C8276M

Angelier, J., Lybéris, N., Le Pichon, X., Barrier, E., & Huchon, P. (1982). The tectonic development of the Hellenic arc and the sea of Crete: A synthesis. *Tectonophysics*, *86*(1–3), 159–196. https://doi.org/10.1016/0040-1951(82)90066-X

Armijo, R., Lyon-Caen, H., & Papanastassiou, D. (1992). East-west extension and Holocene normal-fault scarps in the Hellenic arc. *Geology*, *20*(6), 491–494.

Boore, D. M., Larner, K. L., & Aki, K. (1971). Comparison of two independent methods for the solution of wave-scattering problems: Response of a sedimentary basin to vertically incident *SH* waves. *Journal of Geophysical Research*, *76*(2), 558–569. https://doi.org/10.1029/JB076i002p00558

Breeding, C. M., & Ague, J. J. (2002). Slab-derived fluids and quartz-vein formation in an accretionary prism, Otago Schist, New Zealand. *Geology*, *30*(6), 499. https://doi.org/10.1130/0091-7613(2002)030<0499:SDFAQV>2.0.CO;2

Brooks, M., & Ferentinos, G. (1984). Tectonics and sedimentation in the Gulf of Corinth and the Zakynthos and Kefallinia channels, Western Greece. *Tectonophysics*, *101*(1–2), 25–54. https://doi.org/10.1016/0040-1951(84)90040-4

Brun, J. P., & Faccenna, C. (2008). Exhumation of high-pressure rocks driven by slab rollback. *Earth and Planetary Science Letters*, *272*(1-2), 1–7.

Brüstle, A., Seismicity of the eastern Hellenic Subduction Zone, Ph.D. thesis, Ruhr-University, Bochum, 2012

Caputo, R., Chatzipetros, A., Pavlides, S., & Sboras, S. (2013). The Greek Database of Seismogenic Sources (GreDaSS): State-of-the-art for northern Greece. *Annals of Geophysics*, *55*(5). https://doi.org/10.4401/ag-5168

Carcolé, E., & Sato, H. (2010). Spatial distribution of scattering loss and intrinsic absorption of short-period *S* waves in the lithosphere of Japan on the basis of the multiple lapse time window analysis of Hi-net data. *Geophysical Journal International*, *180*(1), 268–290.

Červený, V., & Soares, J. E. P. (1992). Fresnel volume ray tracing. *Geophysics*, *57*(7), 902–915. https://doi.org/10.1190/1.1443303

D'Alessandro, A., Papanastassiou, D., & Baskoutas, I. (2011). Hellenic Unified Seismological Network: An evaluation of its performance through SNES method. *Geophysical Journal International*, *185*(3), 1417–1430. https://doi.org/10.1111/j.1365-246X.2011.05018.x

Doglioni, C., Agostini, S., Crespi, M., Innocenti, F., Manetti, P., Riguzzi, F., & Savasci, Y. (2002). On the extension in western Anatolia and the Aegean Sea. *Journal of the Virtual Explorer*, *08*. https://doi.org/10.3809/jvirtex.2002.00049

Endrun, B., Meier, T., Bischoff, M., & Harjes, H.-P. (2004). Lithospheric structure in the area of Crete constrained by receiver functions and dispersion analysis of Rayleigh phase velocities. *Geophysical Journal International*, *158*(2), 592–608. https://doi.org/10.1111/j.1365-246X.2004.02332.x

Feuillet, N. (2013). The 2011–2012 unrest at Santorini rift: Stress interaction between active faulting and volcanism. *Geophysical Research Letters*, *40*, 3532–3537. https://doi.org/10.1002/grl.50516

Foucher, J. P., Chamot-Roocke, N., Alexandry, S., Augustin, J. M., Monti, S., Pavlakis, P., & Voisset, M. (1993). *Multibeam bathymetry and seabed reflectivity maps of the MEDRIFF corridor across the eastern Mediterranean Ridge, Terra Cognita (Ed.), EUG (VII)*, (pp. 278–279). London: Blackwell Scientific Publication.

Foutrakis, P. M., & Anastasakis, G. (2018). The active submarine NW termination of the South Aegean active volcanic arc: The Submarine Pausanias Volcanic Field. *Journal of Volcanology and Geothermal Research*, *357*, 399–417. https://doi.org/10.1016/J.JVOLGEORES.2018.05.008

Friederich, W., & Meier, T. (2008). Temporary seismic broadband network acquired data on Hellenic Subduction Zone. *Eos, Transactions American Geophysical Union*, *89*(40), 378–378. https://doi.org/10.1029/2008EO400002

Gallen, S. F., Wegmann, K. W., Bohnenstiehl, D. R., Pazzaglia, F. J., Brandon, M. T., & Fassoulas, C. (2014). Active simultaneous uplift and margin-normal extension in a forearc high, Crete, Greece. *Earth and Planetary Science Letters*, *398*, 11–24. https://doi.org/10.1016/J.EPSL.2014.04.038

Gusev, A. A., & Abubakirov, I. R. (1999a). Vertical profile of effective turbidity reconstructed from broadening of incoherent body-wave pulses-I. General approach and the inversion procedure. *Geophysical Journal International*, *136*(2), 295–308. https://doi.org/10.1046/j.1365-246X.1999.00740.x

Gusev, A. A., & Abubakirov, I. R. (1999b). Vertical profile of effective turbidity reconstructed from broadening of incoherent body-wave pulses-II. Application to Kamchatka data. *Geophysical Journal International*, *136*(2), 309–323. https://doi.org/10.1046/j.1365-246X.1999.00741.x

Halpaap, F., Rondenay, S., & Ottemöller, L. (2018). Seismicity, deformation, and metamorphism in the Western Hellenic Subduction Zone: New constraints from tomography. *Journal of Geophysical Research: Solid Earth*, *123*, 3000–3026. https://doi.org/10.1002/2017JB015154

Hastings, W. K. (1970). Monte Carlo sampling methods using Markov chains and their applications. *Biometrika*, *57*(1), 97–109. https://doi.org/10.1093/biomet/57.1.97

Hatzfeld, D., Besnard, M., Makropoulos, K., & Hatzidimitriou, P. (1993). Microearthquake seismicity and fault-plane solutions in the southern Aegean and its geodynamic implications. *Geophysical Journal International*, *115*(3), 799–818.

Huet, B., Le Pourhiet, L., Labrousse, L., Burov, E., & Jolivet, L. (2011). Post-orogenic extension and metamorphic core complexes in a heterogeneous crust: The role of crustal layering inherited from collision. Application to the Cyclades (Aegean domain). *Geophysical Journal International*, *184*(2), 611–625. https://doi.org/10.1111/j.1365-246X.2010.04849.x

Hukushima, K., & Nemoto, K. (1996). Exchange Monte Carlo method and application to spin glass simulations. *Journal of the Physical Society of Japan*, *65*(6), 1604–1608. https://doi.org/10.1143/JPSJ.65.1604

Hyndman, R. D., McCrory, P. A., Wech, A., Kao, H., & Ague, J. (2015). Cascadia subducting plate fluids channelled to fore-arc mantle corner: ETS and silica deposition. *Journal of Geophysical Research: Solid Earth*, *120*, 4344–4358. https://doi.org/10.1002/2015JB011920

Ishimaru, A. (1978). *Wave propagation and scattering in random media* (Vol. 2, pp. 336–393). New York: Academ. Press.

Jackson, J., & McKenzie, D. (1988). The relationship between plate motions and seismic moment tensors, and the rates of active deformation in the Mediterranean and Middle East. *Geophysical Journal International*, *93*(1), 45–73. https://doi.org/10.1111/j.1365-246X.1988.tb01387.x

Jones, I. F., & Davison, I. (2014). Seismic imaging in and around salt bodies.*Interpretation*, *2*(4), SL1–SL20. https://doi.org/10.1190/INT-2014-0033.1

Karagianni, E. E., Papazachos, C. B., Panagiotopoulos, D. G., Suhadolc, P., Vuan, A., & Panza, G. F. (2005). Shear velocity structure in the Aegean area obtained by inversion of Rayleigh waves.*Geophysical Journal International*, *160*(1), 127–143. https://doi.org/10.1111/j.1365-246X.2005.02354.x

Keay, S., Lister, G., & Buick, I. (2001). The timing of partial melting, Barrovian metamorphism and granite intrusion in the Naxos meta-morphic core complex, Cyclades, Aegean Sea, Greece.*Tectonophysics*, *342*(3–4), 275–312. https://doi.org/10.1016/S0040-1951(01)00168-8

Knapmeyer, M. (1999). Geometry of the Aegean Benioff zones.*Annals of Geophysics*, *42*(1). https://doi.org/10.4401/ag-3697

Knapmeyer, M., & Harjes, H. P. (2000). Imaging crustal discontinuities and the downgoing slab beneath western Crete.*Geophysical Journal International*, *143*(1), 1–21. https://doi.org/10.1046/j.1365-246X.2000.00197.x

Konstantinou, K. I., Evangelidis, C. P., Liang, W.-T., Melis, N. S., & Kalogeras, I. (2013). Seismicity, Vp/Vs and shear wave anisotropy variations during the 2011 unrest at Santorini caldera, southern Aegean.*Journal of Volcanology and Geothermal Research*, *267*, 57–67. https://doi.org/10.1016/j.jvolgeores.2013.10.001

Konstantinou, K. I., Evangelidis, C. P., & Melis, N. S. (2011). The 8 June 2008 *Mw* 6.4 earthquake in Northwest Peloponnese, Western Greece: A case of fault reactivation in an overpressured lower crust?*Bulletin of the Seismological Society of America*, *101*(1), 438–445. https://doi.org/10.1785/0120100074

Konstantinou, K. I., & Melis, N. S. (2008). High-frequency shear-wave propagation across the Hellenic Subduction Zone.*Bulletin of the Seismological Society of America*, *98*(2), 797–803. https://doi.org/10.1785/0120060238

Konstantinou, K. I., Mouslopoulou, V., Liang, W.-T., Heidbach, O., Oncken, O., & Suppe, J. (2017). Present-day crustal stress field in Greece inferred from regional-scale damped inversion of earthquake focal mechanisms.*Journal of Geophysical Research: Solid Earth*, *122*, 506–523. https://doi.org/10.1002/2016JB013272

Le Pichon, X. (1982). Landlocked oceanic basins and continental collision: The Eastern Mediterranean as a case example. In K. Hsü (Ed.), *Mountain Building Processes*, (pp. 201–211). London: Academic Press.

Lee, L. C., & Jokipii, J. R. (1975). Strong scintillations in astrophysics. II. A theory of temporal broadening of pulses.*The Astrophysical Journal*, *201*, 532. https://doi.org/10.1086/153916

Lister, G. S., Banga, G., & Feenstra, A. (1984). Metamorphic core complexes of Cordilleran type in the Cyclades, Aegean Sea, Greece. *Geology*, *12*(4), 221. https://doi.org/10.1130/0091-7613(1984)12<221:MCCOCT>2.0.CO;2

Lomax, A., Virieux, J., Volant, P., & Berge-Thierry, C. (2000). Probabilistic earthquake location in 3D and la yered models. In *Advances in seismic event location* (pp. 101–134). Dordrecht: Springer.

Marini, L., Principe, C., Chiodini, G., Cioni, R., Fytikas, M., & Marinelli, G. (1993). Hydrothermal eruptions of Nisyros (Dodecanese, Greece). Past events and present hazard.*Journal of Volcanology and Geothermal Research*, *56*(1–2), 71–94. https://doi.org/10.1016/0377-0273(93)90051-R

McClusky, S., Balassanian, S., Barka, A., Demir, C., Ergintav, S., Georgiev, I., et al. (2000). Global Positioning System constraints on plate kinematics and dynamics in the eastern Mediterranean and Caucasus.*Journal of Geophysical Research*, *105*(B3), 5695–5719. https://doi.org/10.1029/1999JB900351

Meier, T., Becker, D., Endrun, B., Rische, M., Bohnhoff, M., Stöckhert, B., & Harjes, H.-P. (2007). A model for the Hellenic subduction zone in the area of Crete based on seismological investigations.*Geological Society, London, Special Publications*, *291*(1), 183–199. https://doi.org/10.1144/SP291.9

Meier, T., Rische, M., Endrun, B., Vafidis, A., & Harjes, H. P. (2004). Seismicity of the Hellenic subduction zone in the area of western and central Crete observed by temporary local seismic networks.*Tectonophysics*, *383*(3–4), 149–169. https://doi.org/10.1016/j.tecto.2004.02.004

Melis, N. S., & Tselentis, G.-A. (1998). 3-D *P*-wave velocity structure in Western Greece determined from tomography using earthquake data recorded at the University of Patras Seismic Network (PATNET).*Pure and Applied Geophysics*, *152*). Retrieved from. https://link.springer.com/content/pdf/10.1007%2Fs000240050157.pdf

Mouslopoulou, V., Begg, J., Nicol, A., Oncken, O., & Prior, C. (2015). Formation of Late Quaternary paleoshorelines in Crete, Eastern Mediterranean.*Earth and Planetary Science Letters*, *431*, 294–307. https://doi.org/10.1016/J.EPSL.2015.09.007

Mouslopoulou, V., Nicol, A., Begg, J., Oncken, O., & Moreno, M. (2015). Clusters of megaearthquakes on upper plate faults control the Eastern Mediterranean hazard.*Geophysical Research Letters*, *42*, 10,282–10,289. https://doi.org/10.1002/2015GL066371

Neumann, P., & Zacher, W. (2004). The Cretaceous sedimentary history of the Pindos basin (Greece).*International Journal of Earth Sciences*, *93*(1), 119–131.

Obara, K., & Sato, H. (1995). Regional differences of random inhomogeneities around the volcanic front in the Kanto-Tokai area, Japan, revealed from the broadening of *S* wave seismogram envelopes.*Journal of Geophysical Research*, *100*(B2), 2103–2121. https://doi.org/10.1029/94JB02644

Papazachos, B. C., Dimitriadis, S. T., Panagiotopoulos, D. G., Papazachos, C. B., & Papadimitriou, E. E. (2005). Deep structure and active tectonics of the southern Aegean volcanic arc.*Developments in Volcanology*, *7*, 47–64. https://doi.org/10.1016/S1871-644X(05)80032-4

Papazachos, B. C., Karakostas, V. G., Papazachos, C. B., & Scordilis, E. M. (2000). The geometry of the Wadati-Benioff zone and lithospheric kinematics in the Hellenic arc.*Tectonophysics*, *319*(4), 275–300. https://doi.org/10.1016/S0040-1951(99)00299-1

Papazachos, C. B., Hatzidimitriou, P. M., Panagiotopoulos, D. G., & Tsokas, G. N. (1995). Tomography of the crust and upper mantle in southeast Europe.*Journal of Geophysical Research*, *100*(B7), 12405–12422. https://doi.org/10.1029/95JB00669

Peacock, S. M. (1993). The importance of blueschist → eclogite dehydration reactions in subducting oceanic crust.*Geological Society of America Bulletin*, *105*(5), 684–694. https://doi.org/10.1130/0016-7606(1993)105<0684:TIOBED>2.3.CO;2

Pearce, F. D., Rondenay, S., Sachpazi, M., Charalampakis, M., & Royden, L. H. (2012). Seismic investigation of the transition from conti-nental to oceanic subduction along the western Hellenic Subduction Zone.*Journal of Geophysical Research*, *117*, B07306. https://doi.org/10.1029/2011JB009023

Pik, R., & Marty, B. (2009). Helium isotopic signature of modern and fossil fluids associated with the Corinth rift fault zone (Greece): Implication for fault connectivity in the lower crust.*Chemical Geology*, *266*(1-2), 67–75. https://doi.org/10.1016/J.CHEMGEO.2008.09.024

Pirazzoli, P. A., Thommeret, J., Thommeret, Y., Laborel, J., & Montag-Gioni, L. F. (1982). Crustal block movements from holocene shor-elines: Crete and antikythira (Greece).*Tectonophysics*, *86*(1–3), 27–43. https://doi.org/10.1016/0040-1951(82)90060-9

Piromallo, C., & Morelli, A. (2003). *P* wave tomography of the mantle under the Alpine-Mediterranean area.*Journal of Geophysical Research*, *108*(B2), 2065. https://doi.org/10.1029/2002JB001757

Reilinger, R., McClusky, S., Paradissis, D., Ergintav, S., & Vernant, P. (2010). Geodetic constraints on the tectonic evolution of the Aegean region and strain accumulation along the Hellenic subduction zone.*Tectonophysics*, *488*(1–4), 22–30. https://doi.org/10.1016/J.TECTO.2009.05.027

Reilinger, R., McClusky, S., Vernant, P., Lawrence, S., Ergintav, S., Cakmak, R., et al. (2006). GPS constraints on continental deformation in the Africa-Arabia-Eurasia continental collision zone and implications for the dynamics of plate interactions. *Journal of Geophysical Research*, *111*, B05411. https://doi.org/10.1029/2005JB004051

Saito, T., Sato, H., & Ohtake, M. (2002). Envelope broadening of spherically outgoing waves in three-dimensional random media having power law spectra. *Journal of Geophysical Research*, *107*(B5), 2089. https://doi.org/10.1029/2001JB000264

Saito, T., Sato, H., Ohtake, M., & Obara, K. (2005). Unified explanation of envelope broadening and maximum-amplitude decay of high-frequency seismograms based on the envelope simulation using the Markov approximation: Forearc side of the volcanic front in northeastern Honshu, Japan. *Journal of Geophysical Research*, *110*, B01304. https://doi.org/10.1029/2004JB003225

Sambridge, M. (2014). A parallel tempering algorithm for probabilistic sampling and multimodal optimization. *Geophysical Journal International*, *196*(1), 357–374. https://doi.org/10.1093/gji/ggt342

Sato, H. (1989). Broadening of seismogram envelopes in the randomly inhomogeneous lithosphere based on the parabolic approximation: Southeastern Honshu, Japan. *Journal of Geophysical Research*, *94*(B12), 17735. https://doi.org/10.1029/JB094iB12p17735

Sato, H., Fehler, M. C., & Maeda, T. (2012). *Seismic wave propagation and scattering in the heterogeneous earth* (Vol. 496). Berlin: Springer.

Shaw, B., Ambraseys, N. N., England, P. C., Floyd, M. A., Gorman, G. J., Higham, T. F. G., et al. (2008). Eastern Mediterranean tectonics and tsunami hazard inferred from the AD 365 earthquake. *Nature Geoscience*, *1*(4), 268–276. https://doi.org/10.1038/ngeo151

Shaw, B., & Jackson, J. (2010). Earthquake mechanisms and active tectonics of the Hellenic Subduction Zone. *Geophysical Journal International*, *181*(2), 966–984. https://doi.org/10.1111/j.136

Shiomi, K., Sato, H., & Ohtake, M. (1997). Broad-band power-law spectra of well-log data in Japan. *Geophysical Journal International*, *130*(1), 57–64. https://doi.org/10.1111/j.1365-246X.1997.tb00987.x

Snopek, K., Meier, T., Endrun, B., Bohnhoff, M., & Casten, U. (2007). Comparison of gravimetric and seismic constraints on the structure of the Aegean lithosphere in the forearc of the Hellenic Subduction Zone in the area of Crete. *Journal of Geodynamics*, *44*(3–5), 173–185. https://doi.org/10.1016/j.jog.2007.03.005

Sodoudi, F., Kind, R., Hatzfeld, D., Priestley, K., Hanka, W., Wylegalla, K., et al. (2006). Lithospheric structure of the Aegean obtained from *P* and *S* receiver functions. *Journal of Geophysical Research*, *111*, B12307. https://doi.org/10.1029/2005JB003932

Spakman, W., van der Lee, S., & van der Hilst, R. (1993). Travel-time tomography of the European-Mediterranean mantle down to 1400 km. *Physics of the Earth and Planetary Interiors*, *79*(1–2), 3–74. https://doi.org/10.1016/0031-9201(93)90142-V

Spakman, W., Wortel, M. J. R., & Vlaar, N. J. (1988). The Hellenic Subduction Zone: A tomographic image and its geodynamic implications. *Geophysical Research Letters*, *15*(1), 60–63. https://doi.org/10.1029/GL015i001p00060

Sreenivasiah, I., Ishimaru, A., & Hong, S. T. (1976). Two-frequency mutual coherence function and pulse propagation in a random medium: An analytic solution to the plane wave case. *Radio Science*, *11*(10), 775–778. https://doi.org/10.1029/RS011i010p00775

Stewart, I. S., & Hancock, P. L. (1991). Scales of structural heterogeneity within neotectonic normal fault zones in the Aegean region. *Journal of Structural Geology*, *13*(2), 191–204.

Strobl, M., Hetzel, R., Fassoulas, C., & Kubik, P. W. (2014). A long-term rock uplift rate for eastern Crete and geodynamic implications for the Hellenic subduction zone. *Journal of Geodynamics*, *78*, 21–31. https://doi.org/10.1016/J.JOG.2014.04.002

Suckale, J., Rondenay, S., Sachpazi, M., Charalampakis, M., Hosa, A., & Royden, L. H. (2009). High-resolution seismic imaging of the western Hellenic subduction zone using teleseismic scattered waves. *Geophysical Journal International*, *178*(2), 775–791. https://doi.org/10.1111/j.1365-246X.2009.04170.x

Takahashi, T., Obana, K., Kodaira, S., Suetsugu, D., Takahashi, N., Kamiya, S., & Tamura, Y. (2011). Random inhomogeneities in the northern Izu-Bonin arc estimated by tomographic inversion of peak delay times of *S* wave seismograms. *Journal of Geophysical Research*, *116*, B03303. https://doi.org/10.1029/2010JB007691

Takahashi, T., Obana, K., Yamamoto, Y., Nakanishi, A., Kodaira, S., & Kaneda, Y. (2013). The 3-D distribution of random velocity inhomogeneities in southwestern Japan and the western part of the Nankai subduction zone. *Journal of Geophysical Research: Solid Earth*, *118*, 2246–2257. https://doi.org/10.1002/jgrb.50200

Takahashi, T., Sato, H., & Nishimura, T. (2008). Recursive formula for the peak delay time with travel distance in von Kármán-type non-uniform random media on the basis of the Markov approximation. *Geophysical Journal International*, *173*(2), 534–545. https://doi.org/10.1111/j.1365-246X.2008.03739.x

Takahashi, T., Sato, H., Nishimura, T., & Obara, K. (2007). Strong inhomogeneity beneath Quaternary volcanoes revealed from the peak delay analysis of *S*-wave seismograms of microearthquakes in northeastern Japan. *Geophysical Journal International*, *168*(1), 90–99. https://doi.org/10.1111/j.1365-246X.2006.03197.x

Takahashi, T., Sato, H., Nishimura, T., & Obara, K. (2009). Tomographic inversion of the peak delay times to reveal random velocity fluctuations in the lithosphere: Method and application to northeastern Japan. *Geophysical Journal International*, *178*(3), 1437–1455. https://doi.org/10.1111/j.1365-246X.2009.04227.x

Tatarskii, V. I. (1971). *The effects of the turbulent atmosphere on wave propagation*, (p. 1971). Jerusalem: Israel Program for Scientific Translations.

Tiberti, M. M., Basili, R., & Vannoli, P. (2015). Ups and downs in western Crete (Hellenic Subduction Zone). *Scientific Reports*, *4*(1), 5677. https://doi.org/10.1038/srep05677

Tirel, C., Brun, J.-P., & Burov, E. (2008). Dynamics and structural development of metamorphic core complexes. *Journal of Geophysical Research*, *113*, B04403. https://doi.org/10.1029/2005JB003694

Underhill, J. R. (1988). Triassic evaporites and Plio-Quaternary diapirism in western Greece. *Journal of the Geological Society*, *145*(2), 269–282. https://doi.org/10.1144/gsjgs.145.2.0269

van der Meer, D., van Hinsbergen, D., & Spakman, W. (2017). The Atlas of the underworld: A catalogue of slab remnants in the mantle imaged by seismic tomography, and their geological interpretation. *19th EGU General Assembly, EGU2017, Proceedings from the Conference Held 23-28 April, 2017 in Vienna, Austria., p.3798*, *19*, 3798. Retrieved from http://adsabs.harvard.edu/abs/2017EGUGA..19.3798V

Ventouzi, C., Papazachos, C., Hatzidimitriou, P., & Papaioannou, C. (2018). Anelastic *P*- and *S*-upper mantle attenuation tomography of the southern Aegean Sea subduction area (Hellenic Arc) using intermediate-depth earthquake data. *Geophysical Journal International*, *215*(1), 635–658. https://doi.org/10.1093/gji/ggy292

Wessel, P., Smith, W. H. F., Scharroo, R., Luis, J. F., & Wobbe, F. (2013). Generic mapping tools: Improved version released. *Eos, Transactions American Geophysical Union*, *94*, 409–410.

Wu, R.-S., & Aki, K. (1988). Introduction: Seismic wave scattering in three-dimensionally heterogeneous earth. *Pure and Applied Geophysics Pageoph*, *128*(1–2), 1–6. https://doi.org/10.1007/BF01772587